UNIVERSITA' DI PISA

Facoltà di Ingegneria
Corso di Laurea in Ingegneria Aerospaziale

Hybrid RANS/LES simulations of bluff-body flows

Relatori:

Prof. Maria Vittoria Salvetti

Dott. Ing. Simone Camarri

Candidato:

Gennaro Pagano

ANNO ACCADEMICO 2005-2006

Abstract

A new hybrid RANS/LES approach is presented. The key feature of this approach is a blending between two eddy-viscosities, one given by the $k - \varepsilon$ RANS model and the other by the Smagorinsky VMS-LES (variational multiscale LES) closure. The blending is set by a parameter θ: VMS-LES mode is active when $\theta = 0$, RANS mode if $\theta = 1$, a hybrid mode for $0 < \theta < 1$. The proposed hybrid model is applied first to the numerical simulation of the flow around a square cylinder at $Re_L = 22000$. Three different blending parameters (based on viscosity ratio, time ratio and length ratio) are tested. The results obtained with this new hybrid approach are compared with those obtained using the LNS approach for two different grid resolutions; comparisons with experimental data in the litterature are also provided. The sensitivity of the model to some setting parameters (the inflow value of the turbulent kinetic energy, k_0 and the parameter δ in the approximate wall treatment) is also analysed. The hybrid model is also applied to the simulation of the flow around a circular cylinder at $Re_D = 140000$. The results are compared with those obtained using the DES approach. Also for this case, comparisons with experimental data in the litterature are provided.

Contents

Introduction

Direct Numerical Simulation (DNS) of turbulent flows is feasible only for low Reynolds numbers (Re) due to the required computational resources, which already become prohibitively large for $Re \simeq 10^4$. For this reason, turbulence modeling is a necessary step for the numerical simulation of flows of engineering interest. In this context, the most widely used approach for the simulation of high-Reynolds number turbulent flows is the one based on the discretization of the Reynolds-Averaged Navier-Stokes equations (RANS). In the RANS approach, time averaging is applied to the Navier-Stokes equations and only the time-averaged flow is simulated. In this way a noticeable simplification of the problem is obtained, computational costs are drastically reduced and become almost independent of the Reynolds number when this is sufficiently large. However, RANS simulations usually have difficulties in providing accurate predictions for flows with massive separations, as for instance for the flow around bluff bodies. Indeed, they are in general too dissipative to properly simulate the thrre-dimensional and unsteady phenomena occurring in such flows, yielding to significant discrepancies with respect to the experimental results.

An alternative approach is the Large-Eddy simulation (LES), in which a spatial filter is applied to the equations in order to get rid of small-scale turbulent fluctuations which are thus modeled. The remaining flow scales are directly simulated. Since the dynamics of the large scales is directly simulated and the three-dimensionality and unsteadiness of the flow are naturally taken into account, the LES approach is generally more accurate, but also computationally more expensive, than the RANS one. Moreover, the cost of LES simulations increases as the flow Reynolds number is increased. Indeed, the grid has to be fine enough to resolve a significant part of the turbulent scales, and spatial resolution becomes particularly critical in the near-wall regions.

A new class of models has been recently proposed in the literature in

which the RANS and LES approaches are combined together in order to obtain simulations as accurate as in the LES case but at reasonable computational costs. Among different strategies of combining the two approaches, we consider here the *blending strategy*, in which RANS and LES are blended together in a continuous way throughout the computational domain. This approach leads to the so-called *universal models*.

Among the *universal models* described in the literature, the Detached Eddy Simulation (DES) has received the largest attention. This approach, described in Ref. ([40]), is based on the one-equation Spalart-Allmaras RANS model, in which the length scale of the turbulent kinetic energy destruction term is modified to be the minimum one between the distance to the wall and a length proportional to the local grid resolution. Thus, in the near-wall region and with RANS-like grids the Spalart-Allmaras RANS model is used, while far from the wall the simulation switches to the LES mode with a one-equation SGS closure.

Another hybrid approach, the Limited Numerical Scale (LNS) one, has been recently proposed in Ref. [2]. In this approach, the blending parameter depends on the values of the eddy-viscosity given by a RANS model, μ_t, and of the SGS viscosity given by a LES closure, μ_s. In practice, the minimum of the two eddy-viscosities is used. This should ensure that, where the grid is fine enough to resolve a significant part of the turbulence scales, the model works in the LES mode, while elsewhere the RANS closure is recovered. An example of validation of this hybrid model for the simulation of bluff-body flows is given in Ref. [8].

In the present work, a new strategy is presented for blending RANS and LES approaches in a hybrid model. To this purpose, as proposed in Ref. [22], the flow variables are decomposed in a RANS part (i.e. the averaged flow field), a correction part which takes into account the turbulent large-scale fluctuations, and a third part made of the unresolved or SGS fluctuations. The basic idea of the proposed approach is to solve the RANS equations in the whole computational domain and to correct the obtained averaged flow

field by adding, where the grid is adequately refined, the remaining resolved fluctuations. The equations governing the resolved fluctuations are derived from the RANS and LES equations. Instead of using a zonal approach, in which the regions to be treated by a RANS or LES approach are a-priori defined, as in Ref. [22], a *universal* hybrid model is proposed here. To this aim, a blending function is introduced, θ, which smoothly varies between 0 and 1. The correction term which is added to the averaged flow field is thus damped by a factor $(1-\theta)$, obtaining a model which coincides with the RANS approach when $\theta = 1$ and recovers the LES approach in the limit of $\theta \to 0$. Three different definitions of the blending function θ are proposed, based on the ratios between (i) the two eddy viscosities, (ii) the two characteristic length scales and (iii) the two characteristic time scales given by the RANS and the LES models, respectively. The RANS model used in the proposed hybrid strategy is the standard $k - \varepsilon$ model Ref. [24], for the LES part the Variational Multi-Scale approach (VMS) Ref. [16] is adopted. The VMS approach can be compared in terms of accuracy to the dynamic Smagorinsky model, but its computational cost is definitely lower and comparable to that of the simple Smagorinsky model, as shown in Ref. [18].

The proposed model has been implemented in a numerical solver (AERO) for the Navier-Stokes equations in the case of compressible flows and perfect Newtonian gases, based on a mixed finite-element/finite-volume scheme formulated for unstructured grids made of tetrahedral elements. Finite elements (P1 type) and finite volumes are used to treat the diffusive and convective fluxes, respectively. Concerning the VMS approach, the version proposed in Ref. [18] for compressible flows and for the particular numerical method employed in AERO has been used here.

Also the LNS approach has been implemented in AERO as described in details in Ref. [8], using the standard $k - \varepsilon$ model and the Smagorinky SGS model as the RANS and LES part, respectively.

The capabilities of both the LNS approach and the proposed hybrid approach have been appraised in the simulation of the flow around a square

cylinder at a Reynolds number, based on the far-field velocity and on the side length of the cylinder, equal to $Re = 22000$. For this value of the Reynolds number, several experimental and numerical results are available in the literature (see, for instance, Ref. [26],[4],[3]). Different simulations have been carried out by varying the grid refinement, the inflow value of the turbulent kinetic energy and the free parameter δ in the approximate wall treatment used in AERO, which is based on the Reichardt wall-law Ref. [15]. In the case of the proposed model, all the three different proposals for the blending function θ have been tested. Comparisons with experimental data and numerical results in the literature are also provided.

The new hybrid model has been applied also to the study of the flow around a circular cylinder at a Reynolds number, based on the far-field velocity and on the diameter of the cylinder equal to $Re = 140000$. Also for this kind of flow, several experimental and numerical results are available in the literature (for numerical see, for instance, Ref.[40], for experimental see [1],[20], [19], [34], [33], [31], [10]). This last case has been used to better understand the capability of the new model when the separations is not imposed by the geometry. This is a very important and selective test because a wrong prediction of the separation angle leads to large errors on most quantities of practical interest, such as for instance the aerodynamic forces. Also for this case comparisons with experimental data and numerical results in the literature are also provided.

Chapter 1

Turbulence modeling

1.1 Direct numerical simulation

Turbulent flows are always characterized by an unsteady and tree-dimensional behaviour and can be described by the Naier-Stokes equations.

For a compressible flow, if we consider a thermically and calorically perfect gas and if the body forces are absent or negligible,the governing equations are, using Einstein notation:

$$
\begin{aligned}
\frac{\partial \rho}{\partial t} + \frac{\partial (\rho u_j)}{\partial x_j} &= 0, \\
\frac{\partial (\rho u_i)}{\partial t} + \frac{\partial (\rho u_i u_j)}{\partial x_j} &= -\frac{\partial p}{\partial x_i} + \frac{\partial \sigma_{ij}}{\partial x_j}, \\
\frac{\partial (\rho E)}{\partial t} + \frac{\partial (\rho E u_j)}{\partial x_j} &= -\frac{\partial (p u_j)}{\partial x_j} + \frac{\partial (u_j \sigma_{ij})}{\partial x_i} - \frac{\partial q_j}{\partial x_j}, \\
p &= \rho R T, \\
E &= C_v T + \frac{1}{2} u_i u_i.
\end{aligned}
\tag{1.1}
$$

In the above equations density, temperature, pressure, total energy for unit mass and specific heat at constant volume are represented respectively by ρ, T, p, E and C_v. In the last equation R is equal to $\Re/m$ where $\Re$ is the universal constant of perfect gas and m is the moles mass. By assuming the

flow to be Newtonian and under the Stokes hypothesis, the viscous stress tensor becomes:

$$\sigma_{ij} = -\frac{2}{3}\mu\frac{\partial u_k}{\partial x_k}\delta_{ij} + \mu\Big(\frac{\partial u_i}{\partial x_j} + \frac{\partial u_j}{\partial x_i}\Big) \tag{1.2}$$

where δ_{ij} is the kronecker delta and the viscosity coefficient μ is, generally, a function of the temperature. Moreover, the Fourier law is adopted to model the heat flux:

$$q_i = K\frac{\partial T}{\partial x_i} \tag{1.3}$$

where K is the conduction coefficient for the gas and is generally a function of the temperature. The system of equations above quoted can be numerically integrated for every turbulent flow if an enough fine spatial and temporal resolution is used. Because of the non-linearities of the equation system, the problem is characterized by a large range of spatial and temporal turbulent scales which is function of Reynolds number. The kinetic turbulent energy is excracted by the great scale turbulence and then it is transferred to smaller and smaller scales where is dissipated, as predict by the *Energy Cascade* concept. For this reason in all turbulent flows a continuum spectrum of energy is present. A typical distribution of energy in a turbulent flow as function of the wave-number, n, which is inversely proportional to the spatial scale, is represented in Fig. 1.1.

Fig. 1.1 gives information about the mean-energy of the turbulent structures which have the same dimensions. These structures can be splitted in the following ranges:

- *energy-containing range*, which contains the largest vortical turbulent structures

- *inertial range* or *subrange*, which contains vortices of intermediate dimensions

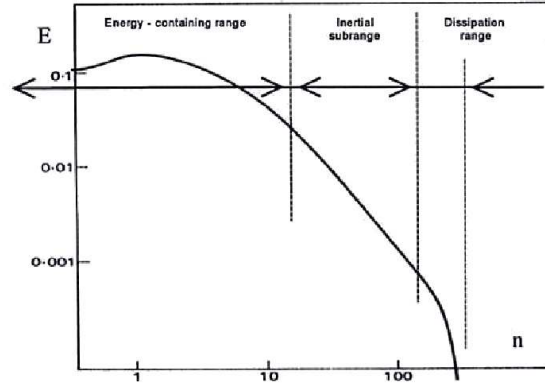- *dissipation range*, which contains the smallest structures.

Figure 1.1.   Typical energy spectrum of a turbulent boundary layer

To estimate the characteristic time and the characteristic dimensions of turbulence, the results of the *Universal Equilibrium Theory* of Kolmogorov Ref. [17] can be used. The spatial orders of magnitude of the largest scales, L, and of the smallest scale in the flow, l_k, are related as follows:

$$\frac{L}{l_k} = Re^{3/4} \tag{1.4}$$

where $Re = \frac{UL}{\nu}$ is the Reynolds number of the flow, based on L and on a integral velocity, which can be assumed similar to the velocity of the largest scales. It can be seen that the separation between large and small scales increases with the Reynolds number. The largest scales of turbulence carry most of the turbulence kinetic energy so they are responsible of the turbulent transport. The smallest scales are responsible of most of the dissipation of kinetic energy, so even if their contribution to the kinetic energy is negligible in comparison with the largest scales they must be considered to obtain accurate results. To this purpose, the single computational cell musts have the dimensions of the smallest turbulent scales and the computational domain must have the dimensions of the largest turbulence scales. Thus, the number of nodes, N, in the whole domain increases with the Reynolds number as follows:

$$N = Re^{9/4} \ . \tag{1.5}$$

As the Reynolds number increases, strong limitations for numerical simulation occur also due to the time resolution requirements. The governing equations, indeed, must be advanced for a global time interval, ΔT_c, of the order of the largest temporal scales, T_c, and the temporal step must be small enough to capture the smallest temporal scales, of the order of t_k. The ratio between the largest and the smallest temporal scales is the following:

$$\frac{T_c}{t_k} = Re^{1/2} \tag{1.6}$$

Thus, if the global time step is constant, the number of temporal steps needed to cover all the range ΔT_c rises quickly with the increase of the Reynolds number.

The huge computational resources needed to directly simulate turbulent flows at high Reynolds numbers ($Re > 10^4$) are not affordable. For this reason, the direct numerical simulation (DNS) is only used for low Reynolds number flows in simple geometries. On the other hand the information which can be obtained in DNS, is much larger than the one required in industrial or engineering problems. Thus, other simplified models have been developed in order to obtain the required information at a significantly reduced computational cost. Reynolds Averaged Navier-Stokes (RANS), Large Eddy Simulation (LES), Detached Eddy Simulation (DES) and Limited Numerical Scales (LNS) are examples of these models.

It is important to stress that, however, DNS gives results that are free of errors due to empirical assumptions made in deriving turbulence models and permits to obtain a large amount of information on turbulence, which is useful to devise and validate turbulent models for the closure of RANS and LES. Thus, DNS plays an important role for the industrial numerical simulation, although indirect.

1.2 Reynolds-Averaged Navier-Stokes equations

The Navier-Stokes equations for compressible flows of (calorically and thermally) perfect Newtonian gases are considered here. These equations write in the conservative form in the following variables: density (ρ), momentum (ρu_i, $i = 1,2,3$) and total energy per unit volume ($E = \rho e + 1/2\rho u_i u_i$, e being the internal energy). The RANS equations are derived by first decomposing the variables (f) in a statistic- or time-average part ($\overline{f}$) and a fluctuant one (f'), this decomposition called the Reynolds decomposition is then introduced in the Navier-Stokes equations which are averaged. Since compressible flows are considered, and in order to suppress correlations of the form $\overline{\rho' f'}$, a density-weighted average (Favre average, $\widetilde{f}$) is also introduced:

$$\widetilde{f} = \frac{\overline{\rho f}}{\overline{\rho}} \quad . \tag{1.7}$$

The averaged flow variables are the unknowns of the RANS problem. However, the RANS equations also contain second-order moments of the flow fluctuations. As well known, these terms must be expressed as a function of the averaged flow variables in order to close the problem. In the present work, the RANS part is closed using the classical $k - \varepsilon$ model and *Low-Reynolds* $k - \varepsilon$ model discussed in the following. The final form of the RANS equations for compressible flows write as follows:

$$\frac{\partial \overline{\rho}}{\partial t} + \left(\overline{\rho}\widetilde{u}_i\right)_{,i} = 0 \quad ,$$

$$\left(\overline{\rho}\widetilde{u}_i\right)_{,t} + \left(\rho\widetilde{u}_i\widetilde{u}_j\right)_{,j} = -\frac{\partial \overline{p}}{\partial i} + \left(\widetilde{\sigma}_{ij} + R_{ij}\right)_{,j} \quad ,$$

$$\left(\overline{E}\right)_{,t} + \left[\widetilde{u}_j\left(\overline{E} + \overline{p}\right)\right]_{,j} = \left[\widetilde{u}_i\widetilde{\sigma}_{ij}\right]_{,j} + \left[\widetilde{u}_i R_{ij}\right]_{,j} + \left[\frac{\mu_t}{\sigma_k}\frac{\partial k}{\partial j}\right]_{,j} +$$

$$\left[C_p\left(\frac{\mu}{Pr} + \frac{\mu_t}{Pr_t}\right)\frac{\partial \widetilde{T}}{\partial j}\right]_{,j} = 0 \quad ,$$

$$\tag{1.8}$$

where $\widetilde{\sigma}_{ij}$ is the averaged viscous-stress tensor, $\overline{E}$ the averaged total energy per unit volume (turbulence included), μ the molecular viscosity of the gas, C_p the specific heat at constant pressure, p the thermodynamic pressure, T the gas temperature, Pr_t the turbulent Prandtl number ($Pr_t = 0.9$ in the present work) and $\mu_{\rm t}$ is the RANS viscosity which depends on the type of closure used (see Sec.1.2.1 or Sec. 1.2.2). Finally, the constitutive equation for $\widetilde{\sigma}_{ij}$ and the averaged state equations of the gas write as follows:

$$\overline{p} = \overline{\rho} R \widetilde{T} \quad , \tag{1.9}$$

$$\widetilde{e} = C_v \widetilde{T} \quad , \tag{1.10}$$

$$\widetilde{\sigma}_{ij} = \mu \widetilde{P}_{ij} \quad , \tag{1.11}$$

where R is the gas constant and C_v its specific heat at constant volume.

1.2.1 Standard $k - \varepsilon$ model

The $k - \varepsilon$ model is an eddy-viscosity model in which the turbulent eddy-viscosity $\mu_{\rm t}$ is defined as a function of the turbulent kinetic energy k and the turbulent dissipation rate of energy ε as follows:

$$\mu_{\rm t} = C_\mu \frac{k^2}{\varepsilon} \quad , \tag{1.12}$$

where C_μ is a constant equal to 0.09. The Reynolds stress tensor is the main unclosed term of the RANS equations, and is modeled according to the Boussinesq assumption:

$$R_{ij} = \overline{\rho \widetilde{u_i' u_j'}} \simeq \mu_{\rm t} \underbrace{\left[\frac{\partial \widetilde{u}_i}{\partial j} + \frac{\partial \widetilde{u}_j}{\partial i} - \frac{2}{3} \frac{\partial \widetilde{u}_k}{\partial k} \delta_{ij} \right]}_{\widetilde{P}_{ij}} - \frac{2}{3} \overline{\rho} k \delta_{ij} \quad , \tag{1.13}$$

δ_{ij} being the Kronecker symbol.

The spatial distribution of k and ϵ is estimated by solving the following transport equation:

$$\frac{\partial \overline{\rho} k}{\partial t} + (\overline{\rho} \widetilde{u}_j k)_{,j} = \left[\left(\mu + \frac{\mu_t}{\sigma_k} \right) \frac{\partial k}{\partial j} \right]_{,j} + R_{ij} \frac{\partial \widetilde{u}_i}{\partial j} - \overline{\rho} \varepsilon \quad , \tag{1.14}$$

$$\frac{\partial \overline{\rho} \varepsilon}{\partial t} + (\overline{\rho} \varepsilon \widetilde{u}_j)_{,j} = \left[\left(\mu + \frac{\mu_t}{\sigma_\epsilon} \right) \frac{\partial \varepsilon}{\partial j} \right]_{,j} + C_{\epsilon 1} \left(\frac{\varepsilon}{k} \right) R_{ij} \frac{\partial \widetilde{u}_i}{\partial j} - C_{\epsilon 2} \overline{\rho} \frac{\varepsilon^2}{k} \tag{1.15}$$

where $C_{\epsilon 1}$, $C_{\epsilon 2}$, σ_k and σ_ϵ are the model parameters and usually are set as follow:

$$C_\epsilon 1 = 1.44 \qquad C_{\epsilon 2} = 1.92 \qquad \sigma_k = 1.0 \qquad \sigma_\epsilon = 1.3$$

1.2.2   Low Reynolds $k - \varepsilon$ model

The Low Reynolds $k - \varepsilon$ model used here is that proposed by Goldberg (Ref. [12]). The Reynolds stress tensor has the same form of that used in the standard $k - \varepsilon$ model (Eq.1.13) but here the turbulent eddy-viscosity μ_t is defined as follows:

$$\mu_t = C_\mu f_\mu \rho \frac{k^2}{\epsilon} \tag{1.16}$$

Here $C_\mu = 0.09$ as in the standard $k - \varepsilon$ model and f_μ is a damping function chosen as follows:

$$f_\mu = \frac{1 - e^{-A_\mu R_t}}{1 - e^{-R_t^{1/2}}} max(1, \psi^{-1}) \tag{1.17}$$

where $\psi = R_t^{1/2}/C_\tau$, $R_t = k^2/(\nu \varepsilon)$, the turbulence Reynolds number, expressed in term of $\nu = \mu/\rho$ and $A_\mu = 0.01$; k and ε are determinated by the following transport equations:

7

$$\frac{\partial \overline{\rho} k}{\partial t} + (\overline{\rho} \widetilde{u}_j k)_{,j} = \left[\left(\mu + \frac{\mu_t}{\sigma_k}\right)\frac{\partial k}{\partial j}\right]_{,j} + R_{ij}\frac{\partial \widetilde{u}_i}{\partial j} - \overline{\rho}\varepsilon \quad , \qquad (1.18)$$

$$\frac{\partial \overline{\rho}\varepsilon}{\partial t} + (\overline{\rho}\varepsilon\widetilde{u}_j)_{,j} = \left[\left(\mu + \frac{\mu_t}{\sigma_\epsilon}\right)\frac{\partial \varepsilon}{\partial j}\right]_{,j} +$$
$$\left(C_{\epsilon 1}R_{ij}\frac{\partial \widetilde{u}_i}{\partial j} - C_{\epsilon 2}\overline{\rho}\varepsilon + E\right)T_\tau^{-1} \quad .$$

$$(1.19)$$

Where T_τ is the realisable time scale and is expressed as follows:

$$T_\tau = \frac{k}{\epsilon}max(1,\psi^{-1}) \qquad (1.20)$$

this time scale is k/ε at large R_t (hence large ψ) but becomes the Kolmogorov scale, $C_\tau(\nu/\varepsilon)^{1/2}$, for $R_t << 1$. The value of C_τ is assumed to be 1.41, $C_{\epsilon 1} = 1.42$, $C_{\epsilon 2} = 1.83$, . The extra source term E in the ε equation is designed such that its near-wall limit cancels the corresponding non-zero destruction term and is computed as follows:

$$E = \rho A_E V (\varepsilon T_\tau)^{0.5}\xi \qquad (1.21)$$

where $A_E = 0.3$, $V = max(\sqrt{k}, (\nu\varepsilon)^{0.25})$ and $\xi = max(\frac{\partial k}{\partial x_i}\frac{\partial \tau}{\partial x_i}, 0)$, with $\tau = k/\varepsilon$.

1.3 Large Eddy Simulation

The large-eddy simulation approach (LES) is intermediate between DNS, where all fluctuations are resolved, and the statistical simulations based on RANS, where only the mean flow is resolved. In LES the severe Reynolds number restrictions of DNS are bypassed by directly simulating the large scales (GS) only and supplying the effect of the missing small scales (SGS) by a so-called sub-grid model. This is obtained by filtering the Navier-Stokes equations in space, in order to eliminate the flow fluctuations smaller then the filter size. In this way, the new unknowns of the problem become the filtered flow variables. Like for RANS, due to the non-linearity of the original problem, the new equations contain additional unknown terms, the so-called sub-grid scale (SGS) terms, representing the effect of the eliminated small scales on the filtered equations. In order to close the problem, these terms must be modelled. However, due to the fact that the small unresolved scales are often simpler in nature than the inhomogeneous large motions, since they do not significantly depend on the large scale motion, rather simple closure models may work well for many applications. Another advantage of this method is the possibility of directly simulating the largest scales, which are usually more interesting from the engineering point of view. Computationally, LES clearly is less demanding than DNS, but in general much more expensive than RANS. The reason is that, independently of the problem to be solved, LES always requires fully three-dimensional and time-dependent calculations even for flows which are two- or one-dimensional in the mean. Moreover LES, like DNS, needs to be carried out for long periods of time to obtain stable and significant statistics. For these reasons, LES should provide better results for the analysis of complex three-dimensional and time-dependent problems for which the RANS approach frequently fails.

The utilization of LES for engineering problems is still not very extensive, but in the last years the interest in this method has largely increased.

1.3.1   SGS modeling

The energy-carrying large scales structures (GS) mainly contribute for the turbulent transport and the dissipative small scale motions (SGS) carry most of the vorticity and act as a sink of turbulent kinetic energy. For high Reynolds numbers the dissipative part of the spectrum becomes clearly separated from the low wave-number range, in a way shown by Eq. (1.4). Some of the significant differences between GS and SGS scales are summarized in Tab. 1.1, Ref. [30].

To illustrate the role of SGS models, it is useful to consider possible con-

GS turbulence	SGS turbulence
Produced by mean flow	Produced by larger eddies
Depends on boundaries	Universal
Ordered	Chaotic
Requires deterministic description	Can be modelled statistically
Inhomogeneous	Homogeneous
Anisotropic	Isotropic
Long-lived	Short-lived
Diffusive	Dissipative
Difficult to model	Easier to model

Table 1.1.   Qualitative differences between GS turbulence and SGS turbulence

sequences if turbulent simulation are performed with insufficient resolution. In this case the viscous dissipation in the flow cannot properly be accounted for. This will typically result in an accumulation of energy at the high wave-number end of the spectrum which reflect a distorted equilibrium state between production and dissipation of turbulent kinetic energy. For sufficiently high Reynolds numbers (or sufficiently coarse grids) the discrete representation of the flow even becomes essentially inviscid and the non-linear transfer of energy can lead to an unbounded growth of turbulence intensities and eventually to numerical instability of the computation.

1.3.2 Filtered equations of the motion

In LES any dependent variable of the flow, f, is split into a GS part, $\overline{f}$, and a SGS part, f':

$$f = \overline{f} + f' \tag{1.22}$$

Generally, the GS component, $\overline{f}$, represents that part of the turbulent fluctuation which remains after some smoothing which has been applied to the flow field.

As done in Sec.1.2 it is convenient define a density weighted filter since it allows to partially recover the formal structure of the equations of the incompressible case. This filter is defined as in Eq.1.7

Applying the filtering operation to the Navier-Stokes equations, Eq. (1.1), yields the equations of motion of the GS flow field. Like in RANS the filtering of the non linearities is of particular interest since it gives rise to additional unknowns terms. For LES of compressible flows, the filtered form of the equations of motion for a thermally and calorically perfect gas is the following:

$$
\begin{aligned}
\frac{\partial \overline{\rho}}{\partial t} + \frac{\partial (\overline{\rho} \tilde{u}_j)}{\partial x_j} &= 0 \\
\frac{\partial (\overline{\rho} \tilde{u}_i)}{\partial t} + \frac{\partial (\overline{\rho} \tilde{u}_i \tilde{u}_j)}{\partial x_j} &= -\frac{\partial \overline{p}}{\partial x_i} + \frac{\partial (\mu \tilde{P}_{ij})}{\partial x_j} - \frac{\partial M_{ij}^{(1)}}{\partial x_j} + \frac{\partial M_{ij}^{(2)}}{\partial x_j} \\
\frac{\partial (\overline{\rho} \tilde{E})}{\partial t} + \frac{\partial [(\overline{\rho} \tilde{E} + \overline{p}) \tilde{u}_j]}{\partial x_j} &= \frac{\partial (\tilde{u}_j \tilde{\sigma}_{ij})}{\partial x_i} - \frac{\partial \tilde{q}_j}{\partial x_j} + \frac{\partial}{\partial x_j} \left(Q_j^{(1)} + Q_j^{(2)} + Q_j^{(3)} \right).
\end{aligned}
\tag{1.23}
$$

In the momentum equation the sub-grid terms are represented by the terms $M_{ij}^{(i)}$ which can be defined as follows:

$$
\begin{aligned}
M_{ij}^{(1)} &= \overline{\rho u_i u_j} - \overline{\rho} \tilde{u}_i \tilde{u}_j \tag{1.24} \\
M_{ij}^{(2)} &= \overline{\mu P_{ij}} - \mu \tilde{P_i} j \tag{1.25}
\end{aligned}
$$

and

$$P_{ij} = -\frac{2}{3} S_{kk} \delta_{ij} + 2S_{ij} \tag{1.26}$$

where S_{ij} is the strain rate tensor defines as:

$$S_{ij} = \frac{1}{2}\left(\frac{\partial u_i}{\partial x_j} + \frac{\partial u_j}{\partial x_i}\right) . \tag{1.27}$$

$M_{ij}^{(1)}$ takes into account the momentum transport of the sub-grid scales and $M_{ij}^{(2)}$ represents the transport of viscosity due to the sub-grid scales fluctuations.

In the energy equation the sub-grid term are represented by the terms $Q_j^{(i)}$ which can be defined as follows:

$$Q_j^{(1)} = \left[\tilde{u}_i\left(\overline{\rho}\tilde{E} + \overline{p}\right) - \overline{u_i(\rho E + p)}\right] \tag{1.28}$$

$$Q_j^{(2)} = \overline{\left(\mu P_{ij} u_j\right)} - \left(\mu \tilde{P}_{ij}\tilde{u}_j\right) \tag{1.29}$$

$$Q_j^{(3)} = \overline{K\frac{\partial T}{\partial x_j}} - K\frac{\partial \tilde{T}}{\partial x_j} \tag{1.30}$$

$Q_j^{(1)}$ represents three distinct physical effects:

- the transport of energy E due to small scales fluctuations;

- the change of the internal energy due to the sub-grid scale compressibility $\left(p\frac{\partial u_j}{\partial x_j}\right)$;

- the dissipation of energy due to sub-grid-scale motions in the pressure field $\left(u_j\frac{\partial p}{\partial x_j}\right)$;

$Q_j^{(2)}$ takes in account the dissipative effect due to the sub-grid scale transport of viscosity; $Q_j^{(3)}$ takes in account the heat transfer caused by the motion of the neglected sub-grid scales.

1.3.3 Smagorinsky's model

The Smagorinsky model is an example of closure models (ref.[36]). We assume that low compressibility effects are present in the SGS fluctuations and that heat transfer and temperature gradients are moderate. The retained SGS term in the momentum equation is thus the classical SGS stress tensor:

$$M_{ij} = \rho \overline{u_i u_j} - \bar{\rho} \tilde{u}_i \tilde{u}_j \qquad (1.31)$$

where the over-line denotes the grid filter and the tilde the density-weighted Favre filter (Eq.1.7). The isotropic part of M_{ij} can be neglected under the assumption of low compressibility effect in the SGS fluctuations. The deviatoric part, T_{ij}, may be expressed by an eddy viscosity term, in accordance with the Smagorinsky model extended to compressible flow:

$$\begin{aligned} T_{ij} &= -2\mu_s \left(\tilde{S}_{ij} - \frac{1}{3}\tilde{S}_{kk} \right), & (1.32) \\ \mu_s &= \bar{\rho} C_s \Delta^2 |\tilde{S}|. & (1.33) \end{aligned}$$

where $\tilde{S}_{ij}$ is the resolved strain rate tensor, μ_s is the SGS viscosity, Δ is the filter width, C_s is a constant which must be assigned a priori and $|\tilde{S}| = \sqrt{\tilde{S}_{ij}\tilde{S}_{ij}}$. The width of the filter is defined for every grid elements, l, as follows:

$$\Delta^{(l)} = Vol_j^{1/3} \qquad (1.34)$$

where Vol_j is the volume of the $j-th$ grid element.

In the energy equation the effect of the SGS fluctuations has been modified by the introduction of a constant SGS Prandtl number to be assigned a priori:

$$Pr_{sgs} = C_p \frac{\mu_s}{K_{sgs}} \qquad (1.35)$$

where K_{sgs} is the SGS conductivity coefficient and it takes into account the diffusion of total energy caused by the SGS fluctuation. In the filtered energy

equation, the term K_{sgs} is added to the molecular conductivity coefficient. Another limit for LES is due to the assumption frequently made in SGS modeling that the cut-off of the filter is in the inertial range and this, for high Reynolds flows, implies huge computational costs.

1.4 Limited Numerical Scales

While LES is an increasingly powerful tool for unsteady turbulent flow prediction, it is still prohibitively expensive. To bring LES closer to becoming a design tool, hybrid RANS/LES approaches have been developed. One of these is based on Limited Numerical Scales (LNS) which combines RANS and LES in a single modeling framework. This approach has the advantage of being particularly easy to be implemented in existing codes. In LNS the Reynolds tensor is modeled by an eddy-viscosity which is obtained by taking the minimum value between the ones given respectively by RANS k-ϵ model and by the LES Smagorinsky model. This should, in principle, allow the LES approach to be used where the grid resolution is adequate for resolving the largest turbulence scales, while the RANS approach is used where the grid is not sufficiently refined. Howevere, this model, as all the hybrid models, is mainly based on empiricism.

In the LNS model the Reynolds stress tensor given by the RANS closure is multiplied by a blending function. Thus, the LNS equations are obtained from the RANS ones by replacing the Reynolds stress tensor R_{ij}, given by Eq. (1.13), with the tensor L_{ij}:

$$L_{ij} = \alpha R_{ij} = \alpha \mu_t \widetilde{P}_{ij} - \frac{2}{3}\overline{\rho}\left(\alpha k\right)\delta_{ij} \quad , \tag{1.36}$$

where α is the damping function $(0 \leq \alpha \leq 1)$, varying in space and time.

In the LNS model proposed in [2], the damping function is defined as follows:

$$\alpha = \min\left\{\frac{\mu_s}{\mu_t}, 1\right\} \tag{1.37}$$

in which μ_s is the SGS viscosity obtained from a LES closure model. The Smagorinsky SGS model (sec. 1.3.3) is adopted here.

The set of LNS equations is reported here for sake of completeness:

$$\frac{\partial \overline{\rho}}{\partial t} + \frac{\partial \overline{\rho}\widetilde{u}_i}{\partial x_i} = 0 \quad , \tag{1.38}$$

$$\frac{\partial \overline{\rho}\widetilde{u}_i}{\partial t} + \frac{\partial \rho \widetilde{u}_i \widetilde{u}_j}{\partial x_j} = -\frac{\partial \overline{p}}{\partial x_i} + \frac{\partial (\widetilde{\sigma}_{ij} + L_{ij})}{\partial x_j} \quad , \tag{1.39}$$

$$\frac{\partial \overline{E}}{\partial t} + \frac{\partial \widetilde{u}_j \left(\overline{E} + \overline{p} \right)}{\partial x_j} = \frac{\partial \widetilde{u}_i \widetilde{\sigma}_{ij}}{\partial x_j} + \frac{\partial \widetilde{u}_i L_{ij}}{\partial x_j} + \frac{\partial}{\partial x_j} \left(\frac{\alpha \mu_{\mathrm{t}}}{\sigma_k} \frac{\partial k}{\partial x_j} \right) +$$
$$\frac{\partial}{\partial x_j} \left(\frac{C_p}{Pr} \left(\mu + \alpha \mu_{\mathrm{t}} \right) \frac{\partial \widetilde{T}}{\partial x_j} \right) = 0 \tag{1.40}$$

$$\frac{\partial \overline{\rho}k}{\partial t} + \frac{\partial \overline{\rho}\widetilde{u}_j k}{\partial x_j} = \frac{\partial}{\partial x_j} \left[\left(\mu + \frac{\alpha \mu_{\mathrm{t}}}{\sigma_k} \right) \frac{\partial k}{\partial x_j} \right] + L_{ij} \frac{\partial \widetilde{u}_i}{\partial x_j} - \overline{\rho}\varepsilon \quad , \tag{1.41}$$

$$\frac{\partial \overline{\rho}\varepsilon}{\partial t} + \frac{\partial \overline{\rho}\varepsilon\widetilde{u}_j}{\partial x_j} = \frac{\partial}{\partial x_j} \left[\left(\mu + \frac{\alpha \mu_{\mathrm{t}}}{\sigma_\epsilon} \right) \frac{\partial \varepsilon}{\partial x_j} \right] + C_{\epsilon 1} \left(\frac{\varepsilon}{k} \right) L_{ij} \frac{\partial \widetilde{u}_i}{\partial x_j} -$$
$$C_{\epsilon 2} \overline{\rho} \frac{\varepsilon^2}{k} \quad . \tag{1.42}$$

in which p is the pressure, σ_{ij} the viscous-stress tensor, μ the molecular viscosity, C_p the specific heat at constant pressure, T the temperature and Pr_t the turbulent Prandtl number. The values have used for the different parameters in the k and ε equations are that of Sec.1.2.

Summarizing, wherever the LES SGS-viscosity is lower than the RANS eddy-viscosity ($\alpha < 1$), an expression very similar to the classical Smagorinsky model is obtained for the turbulent stresses by combining Eqs. (1.13), (1.36) and(1.37). The difference with the classical Smagorinsky model is the presence of the diagonal term proportional to k. However, for compressible flows, this can be considered as a model for the isotropic part of the SGS stresses. As discussed previously and in ref. [2], the model should work in the LES mode where the grid is fine enough to resolve a significant part of the turbulence scales, as in LES; elsewhere ($\alpha = 1$), the $k - \varepsilon$ RANS closure is recovered.

Note that in LNS R_{ij} is replaced with L_{ij} not only in the momentum and energy equations, but also in the two additional equations in k and ε. This implies that, although the total turbulent kinetic energy dissipates at the rate dictated by ε, the energy-production term $R_{ij} \frac{\partial \widetilde{u}_i}{\partial j}$ is replaced by

$L_{ij}\frac{\partial \widetilde{u}_i}{\partial j} = \alpha R_{ij}\frac{\partial \widetilde{u}_i}{\partial j}$. Consequently, a reduction of the turbulent kinetic energy production is obtained in those regions where a fraction of turbulence is directly simulated ($\alpha < 1$).

A reduction of the turbulent transport of k and ε in regions where $\alpha < 1$ is also obtained by replacing μ_t with $\alpha\mu_t$ in the RANS equations for k and ε.

Finally, one can notice that, by construction, the present version of the LNS model is no more time consuming than the RANS $k - \epsilon$ model. Indeed, the extra-cost due to the evaluation of the Smagorinsky eddy viscosity is negligible compared to the overall computation required by the solution of the RANS $k - \epsilon$ equations.

1.5   Detached Eddy Simulation

A Detached Eddy Simulation is a three-dimensional unsteady numerical solver using a single turbulence model, which works as a sub-grid-scale model in regions where the grid density is fine enough for a large-eddy simulation, and as a Reynolds-averaged model in elsewhere.The model senses the grid density and, where it is enough refined, adjusts itself to a lower level of mixing, with respect to the "RANS mode", in order to unlock the larger-scale instabilities of the flow and to let the energy cascade extend to length scales close to the grid spacing. In other regions, primarily boundary layers, the model works in RANS mode (however the computed solution is generally unsteady also in this region). There is a single velocity and model field, and no issue of smoothness between regions. The formulation is based on the the following one-equation S-A model([38]). This model solves only one transport equation for the quantity $\widetilde{\nu}$, which is equivalent to the kinematic eddy viscosity ν_t far from walls. The transport equation has been constructed empirically to reproduce flows of increasing complexity. The transport equation, neglecting transition term, reads ([37])

$$\frac{D\widetilde{\nu}}{Dt} = c_{b1}\widetilde{S}\widetilde{\nu} - c_{w1}f_w(\frac{\widetilde{\nu}}{d})^2 + \frac{1}{\sigma}[div([\widetilde{\nu} + \nu]grad\widetilde{\nu}) + c_{b2}grad\widetilde{\nu}.grad\widetilde{\nu}] \quad (1.43)$$

where d is the distance to the nearest wall. The model has been tuned so that, close to solid surfaces but outside the viscous sub-layer, it fits the logarithmic region, i.e.

$$\widetilde{\nu} = u_\tau \kappa d, \quad \widetilde{S} = \frac{u_\tau}{\kappa d} \quad (1.44)$$

where u_τ is the friction velocity based upon the wall friction τ_w ($u_\tau = (\tau_w/\rho)^{1/2}$) and κ is the von Karman constant. The turbulent viscosity ν_t is linked to the transported variable $\widetilde{\nu}$ by

$$\nu_t = f_{v1}\widetilde{\nu}, \quad f_{v1} = \frac{\chi^3}{\chi^3 + c_{v1}^3}, \quad \chi = \frac{\widetilde{\nu}}{\nu} \quad (1.45)$$

and $\widetilde{S}$ is linked to the vorticity S (which reduces to $|\frac{\partial u}{\partial y}|$ in thin shear flows), by

$$\widetilde{S} = S + \frac{\widetilde{\nu}}{\kappa^2 d^2} f_{v2}, \quad f_{v2} = 1 - \frac{\chi}{1 + \chi f_{v1}} \tag{1.46}$$

Finally, f_w is a function of the ratio $r = \widetilde{\nu}/(\widetilde{S}\kappa^2 d^2)$, and both equal unity in the log layer. Eq.1.43 is in balance provided that $c_{w1} = c_{b1}/\kappa^2 + (1 + c_{b2})/\sigma$. In the DES model (Ref.[40]), the only modification consists in substituting for d, everywhere in the equations, the new length scale $\widetilde{d}$. This depends on the grid spacing Δ:

$$\widetilde{d} = min(d, C_{DES}\Delta) \tag{1.47}$$

where Δ is based on the largest dimension of the grid cell, i.e.:

$$\Delta = max(\Delta x, \ \Delta y, \ \Delta z). \tag{1.48}$$

for structured grids (Ref. [40]) and assuming that the coordinates (x,y,z) are alligned with the grid cell. For unstructured grids Δ is equal to the diameter of the grid cell, divided by $3^{1/2}$. The empirical constant C_{DES} is equal to 0.65, and is not very critical Ref.[40].

1.6   New Hybrid Model

As in ref. [22], the following decomposition of the flow variables is adopted:

$$w_i = \underbrace{< w_i >}_{RANS} + \underbrace{w_i^c}_{correction} + w_i{}^{SGS}$$

where $< w_i >$ are the flow variables in RANS, obtained by applying an averaging operator to the Navier-Stokes equations, w_i^c are the remaining resolved fluctuations (i.e. $< w_i > +w_i^c$ are the flow variables in LES) and $w_i{}^{SGS}$ are the unresolved or SGS fluctuations.

If we write the Navier-Stokes equations in the following compact conservative form:

$$\frac{\partial \boldsymbol{W}}{\partial t} + \nabla \cdot F(\boldsymbol{W}) = 0$$

in which F represents both the viscous and the convective fluxes, for the averaged flow $\langle \boldsymbol{W} \rangle$ we get:

$$\frac{\partial \langle \boldsymbol{W} \rangle}{\partial t} + \nabla \cdot F(\langle \boldsymbol{W} \rangle) = -\tau^{RANS}(\langle \boldsymbol{W} \rangle) \tag{1.49}$$

where $\tau^{RANS}(\langle \boldsymbol{W} \rangle)$ is the closure term given by a RANS turbulence model.

As well known, by applying a filtering operator to the Navier-Stokes equations, the LES equations are obtained, which, in the previously introduced notations, can be written:

$$\frac{\partial \langle \boldsymbol{W} \rangle + \boldsymbol{W}^c}{\partial t} + \nabla \cdot F(\langle \boldsymbol{W} \rangle + \boldsymbol{W}^c) = -\tau^{LES}(\langle \boldsymbol{W} \rangle + \boldsymbol{W}^c) \tag{1.50}$$

where τ^{LES} is the SGS term.

An equation for the resolved fluctuations $\boldsymbol{W}^c$ can thus be derived as follows (see also ref. [22]):

$$\frac{\partial \boldsymbol{W}^c}{\partial t} + \nabla \cdot F(\langle \boldsymbol{W} \rangle + \boldsymbol{W}^c) - \nabla \cdot F(\langle \boldsymbol{W} \rangle) = \tau^{RANS}(\langle \boldsymbol{W} \rangle) - \tau^{LES}(\langle \boldsymbol{W} \rangle + \boldsymbol{W}^c) \tag{1.51}$$

The basic idea of the proposed hybrid model is to solve Eq. (1.49) in the whole domain and to correct the obtained averaged flow by adding the remaining resolved fluctuations (computed through Eq. (1.51)), wherever the grid resolution is adequate for a LES. Instead of using a zonal approach as in [22], in which the regions where the additional fluctuations that must be computed are a priori defined, we wish to construct a *universal* hybrid model. To this aim, we introduce a *blending function*, θ, smoothly varying between 0 and 1. When $\theta = 1$, no correction to $\langle \boldsymbol{W} \rangle$ is computed and, thus, the RANS approach is recovered. Conversely, wherever $\theta < 1$, additional resolved fluctuations are computed; in the limit of $\theta \to 0$ we want to recover a full LES approach. The definition of the blending function is discussed in details in Sec. 1.6.1. Thus, wherever $\theta < 1$, we also solve the following equation for the fluctuations:

$$
\frac{\partial \boldsymbol{W}^c}{\partial t} \;+\; \nabla \cdot F(\langle \boldsymbol{W} \rangle + \boldsymbol{W}^c) \;-\; \nabla \cdot F(\langle \boldsymbol{W} \rangle) \;=\;
$$

$$
(1 - \theta) \left[\tau^{RANS}(\langle \boldsymbol{W} \rangle) - \tau^{LES}(\langle \boldsymbol{W} \rangle + \boldsymbol{W}^c) \right]
$$

(1.52)

Note that for $\theta \to 1$ the RANS limit is actually recovered; indeed, for $\theta = 1$ the right-hand side of Eq. (1.52) vanishes and, hence, a trivial solution is $\boldsymbol{W}^c = 0$. As required, for $\theta = 0$ Eq. (1.52) becomes identical to Eq. (1.51) and the remaining resolved fluctuations are added to the averaged flow; the model, thus, works in LES mode. For θ going from 1 to 0, i.e. when, following the definition of the blending function (see Sec. 1.6.1), the grid resolution is intermediate between one adequate for RANS and one adequate for LES, the righthand side term in Eq. (1.52) is damped through multiplication by $(1 - \theta)$. Although it could seem rather arbitrary from a physical point of view, this is aimed, as said before, to obtain a smooth transition between RANS and LES. More specifically, we wish to obtain a progressive addition of fluctuations when the grid resolution increases and the model switches from the RANS to the LES mode, in order to try to overcome the well known

problems of existing universal hybrid models in the transition from RANS to LES, as, for instance, the "gray zones" in DES or the need of addition of synthetic turbulence in LNS (ref.[2]).

Summarizing, the ingredients of the proposed approach are: a RANS closure model, a SGS model for LES and the definition of the blending function. As far the closure of the RANS equations is concerned, in the present study, the standard $k - \varepsilon$ model discussed in sec.1.2.1 is used for the simulation around the square cylinder, and the low Reynolds $k - \varepsilon$ (sec.1.2.2) model for the circular cylinder. For the LES mode, we wish to recover the variational multi scale approach which will be described in Sec.2.4.

1.6.1   Definition of the blending function

As a possible choice for θ, the following function is used in the present study:

$$\theta = F(\xi) = tanh(\xi^2) \tag{1.53}$$

where ξ is the *blending parameter*, which should indicate whether the grid resolution is fine enough to resolve a significant part of the turbulence fluctuations, i.e. to obtain a LES-like simulation. The choice of the *blending parameter* is clearly a key point for the definition of the present hybrid model. In the present study, different options are proposed and investigated, namely:

- $\xi = \dfrac{\mu_s}{\mu_t}$, which is also used as a blending parameter in LNS [2],

- $\xi = \dfrac{\Delta}{l_{RANS}}$, l_{RANS} being a typical length in the RANS approach, i.e.
  $l_{RANS} = \dfrac{k^{3/2}}{\epsilon}$

- $\xi = \dfrac{t_{LES}}{t_{RANS}}$, t_{LES} and t_{RANS} being characteristic times of the LES and RANS approaches respectively, $t_{LES} = \dfrac{1}{\sqrt{S'_{ij}S'_{ij}}}$ and $t_{RANS} = \dfrac{k}{\epsilon}$.

Chapter 2

Numerical Method

2.1 Introduction

In the present chapter the code AERO, used in the present study, is described. The code permits to solve the Euler equations, the Navier Stokes equations for laminar flows and to use different turbulence models for RANS, LES and hybrid RANS/LES approaches. The unknown quantities are the density, the components of the momentum and the total energy per unit volume. AERO employs a mixed finite-volume/finite-element formulation for the spatial discretization of the equations. Finite-volumes are used for the convective fluxes and finite-elements (P1) for the diffusive ones. The resulting scheme is second order accurate in space. The equations can be advanced in time with explicit low-storage Runge-Kutta schemes. Also implicit time advancing is possible, based on a linearized method that is second order accurate in time.

2.2 Set of equations

In the AERO code the Navier Stokes equations are numerically normalized with the following reference quantities:

- $L_{ref} \implies$ characteristic length of the flow

- $U_{ref} \implies$ velocity of the free-stream flow

- $\rho_{ref} \implies$ density of the free-stream flow

- $\mu_{ref} \implies$ molecular viscosity of the free-stream flow

The flow variables can be normalized with the reference quantities as follows:

$$\rho^* = \frac{\rho}{\rho_{ref}} \qquad u_j^* = \frac{u_j}{U_{ref}} \qquad p^* = \frac{p}{p_{ref}}$$

$$E^* = \frac{E}{\rho_{ref}U_{ref}^2} \qquad \mu^* = \frac{\mu}{\mu_{ref}} \qquad t^* = t\,\frac{L_{ref}}{U_{ref}} \; . \tag{2.1}$$

The non-dimensional form of the Navier Stokes equations can be obtained substituting the reference quantities Eq. (2.1) in the set of equations described in Eq. (1.1). As an example the non-dimensional equations for the laminar case are reported in the following:

$$
\begin{aligned}
\frac{\partial \rho^*}{\partial t^*} + \frac{\partial(\rho^* u_j^*)}{\partial x_j^*} &= 0 \\
\frac{\partial(\rho^* u_i^*)}{\partial t^*} + \frac{\partial \rho^* u_i^* u_j^*}{\partial x_j^*} &= -\frac{\partial p^*}{\partial x_i^*} + \frac{1}{Re}\frac{\partial \sigma_{ij}^*}{\partial x_j^*} \\
\frac{\partial(\rho^* E^*)}{\partial t^*} + \frac{\partial(\rho^* E^* u_j^*)}{\partial x_j^*} &= -\frac{\partial(p^* u_j^*)}{\partial x_j^*} + \frac{1}{Re}\frac{\partial(u_j^* \sigma_{ij}^*)}{\partial x_i^*} - \frac{\gamma}{RePr}\frac{\partial}{\partial x_j^*}\left[\mu^*\left(E^* - \frac{1}{2}u_j^* u_j^*\right)\right]
\end{aligned}
\tag{2.2}
$$

where the Reynolds number, $Re = U_{ref}L_{ref}/\nu$, is based on the references quantities, U_{ref} and L_{ref}, the Prandlt number, Pr, can be assumed constant for a gas and equal to:

$$Pr = \frac{C_p \mu}{k}$$

and $\gamma = C_p/C_v$ is the ratio between the specific heats at constant pressure and volume. Also the constitutive equations for the viscous stresses and the state equations may be written in non-dimensional form as follows:

$$\sigma_{ij}^* = -\frac{2}{3}\mu^*\left(\frac{\partial u_k^*}{\partial x_k^*}\delta_{ij}\right) + \mu^*\left(\frac{\partial u_i^*}{\partial x_j^*} + \frac{\partial u_j^*}{\partial x_i^*}\right)$$

$$p^* = (\gamma - 1)\rho^*\left(E^* - \frac{1}{2}u_j^* u_j^*\right) . \tag{2.3}$$

In order to rewrite the governing equations in a compact form more suitable for the discrete formulation, we group together the unknown variables in the $\boldsymbol{W}$ vector:

$\boldsymbol{W} = (\rho,\ \rho u,\ \rho v,\ \rho w,\ \rho E)^T$.

If we define the two vectors, $\boldsymbol{F}$ and $\boldsymbol{V}$ as function of $\boldsymbol{W}$, as follows:

$$\boldsymbol{F} = \begin{pmatrix} \rho u & \rho v & \rho w \\ \rho u^2 + p & \rho uv & \rho uw \\ \rho uv & \rho v^2 + p & \rho vw \\ \rho uw & \rho vw & \rho w^2 + p \end{pmatrix}$$

and

$$\boldsymbol{V} = \begin{pmatrix} 0 & 0 & 0 \\ \sigma_{xx} & \sigma_{yx} & \sigma_{zx} \\ \sigma_{xy} & \sigma_{yy} & \sigma_{zy} \\ \sigma_{xz} & \sigma_{yz} & \sigma_{zz} \\ u\sigma_{xx} + v\sigma_{xy} + w\sigma_{xz} - q_x & u\sigma_{xy} + v\sigma_{yy} + w\sigma_{yz} - q_y & u\sigma_{xz} + v\sigma_{yz} + w\sigma_{zz} - q_z \end{pmatrix}$$

and if we substitute the vectors $\boldsymbol{V}$ and $\boldsymbol{F}$ in (2.2), it is possible to rewrite the governing equations in the following compact format, which is the starting point for the derivation of the Galerkin formulation and of the discretization of the problem:

$$\frac{\partial \boldsymbol{W}}{\partial t} + \frac{\partial}{\partial x_j}F_j(\boldsymbol{W}) - \frac{1}{Re}\frac{\partial}{\partial x_j}V_j(\boldsymbol{W}, \nabla\boldsymbol{W}) = 0 . \tag{2.4}$$

One can note that the vectors $\boldsymbol{F}$ and $\boldsymbol{V}$ are respectively the convective fluxes and the diffusive fluxes.

2.3   Space discretization

Spatial discretization is based on a mixed finite-volume/finite-element formulation. A finite volume upwind formulation is used for the treatment of the convective fluxes while a classical Galerkin finite-element centered approximation is employed for the diffusive terms .

The computational domain Ω is approximated by a polygonal domain Ω_h. This polygonal domain is then divided in N_t tetrahedrical elements T_i by a standard finite-element triangulation process:

$$\Omega_h = \bigcup_{i=1}^{N_t} T_i. \tag{2.5}$$

The set of elements T_i forms the grid used in the finite-element formulation. The dual finite-volume grid can be built starting from the triangulation following two ways: the Barth cell construction (BC) or the medians method. The first one is useful for significantly stretched grids. This type of cells can be obtained in 3D as follows: to build the cell centered at node i, let us consider all the neighboring nodes of i (j). For each element containing the nodes i and j, the cell surface is given by the triangles connecting the middle of the edge joining these two vertices, the *surface center* of the faces of the element having this edge in common, and the *volume center* of the element. The *surface center* of a given face is the center of its circumscribed circle, if the face comprises only acute angles, otherwise it is the middle of its longest edge, and the *volume center* of an element is the center of its circumscribed sphere if the former is located inside the element, otherwise, it is the surface center (among those of the four tetrahedorn faces), which is closest to the center of the circumscribed sphere. Although the BC can be built starting from a generic tetrahedrization, it is interesting to consider the case of a Cartesian mesh, thus, made of rectangle parallelepipeds (thereafter called *bricks*), which are cut in a particular way in tetrahedrons, following [13]. This division splits each brick in six identical tetrahedra, each being the mirror image of its neighbors (called also *English flag* division see Fig.

2.1(a)). Starting from such a tetrahedization, the BC cells are bricks, centered around the vertices of the mesh, as can be seen in Fig. 2.1b, in which the trace of the division of an element into BC is shown.
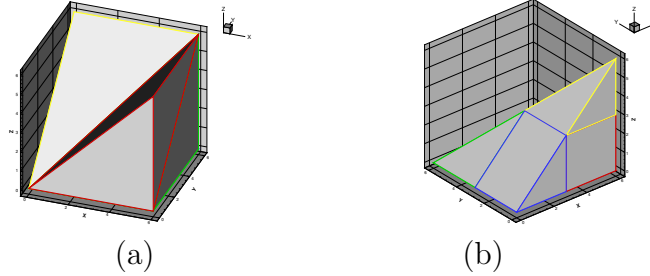

(a)   (b)

Figure 2.1.   New finite-volume cells in 3D: (a) division in tetrahedrons, (b) trace of BC on a tetrahedron resulting from the previous division.

In the medians method a finite-volume cell is constructed around each node a_i of the triangulation, dividing in 4 sub-tetrahedra every tetrahedron having a_i as a vertex by means of the median planes. We will call C_i the union of the resulting sub-tetrahedra having a_i as a vertex and they have the following property:

$$\Omega_h = \bigcup_{i=1}^{N_c} C_i. \tag{2.6}$$

where N_c is the number of cells, which is equal to the number of the nodes of the triangulation.

Convective fluxes

If we indicate the basis functions for the finite-volume formulation as follows:

$$\psi^{(i)}(P) = \begin{cases} 1 & \text{if } P \in C_i \\ 0 & \text{otherwise} \end{cases}$$

the Galerkin formulation for the convective fluxes is obtained by multiplying the convective terms of (2.4) by the basis function $\psi^{(i)}$, integrating on the domain Ω_h and using the divergence theorem. In this way we obtain:

27

$$\iint_{\Omega_h} \left(\frac{\partial F_j}{\partial x_j}\right)\psi^{(i)}\, \mathrm{d}x\, \mathrm{d}y = \iint_{C_i} \frac{\partial F_j}{\partial x_j}\, \mathrm{d}\Omega = \int_{\partial C_i} F_j n_j\, \mathrm{d}\sigma$$

where $d\Omega$, $d\sigma$ and n_j are the elementary measure of the cell, of its boundary and the jth component of the normal external to the cell C_i respectively. The total contribution to the convective fluxes is:

$$\sum_j \int_{\partial C_{ij}} \mathcal{F}(\boldsymbol{W},\vec{n})\, \mathrm{d}\sigma$$

where j are all the neighboring nodes of i, $\mathcal{F}(\boldsymbol{W},\vec{n}) = F_j(\boldsymbol{W})n_j$, ∂C_{ij} is the boundary between cells C_i and C_j, and $\vec{n}$ is the outer normal to the cell C_i.

The basic component for the approximation of the convective fluxes is the Roe scheme, Ref. [32]:

$$\int_{\partial C_{ij}} \mathcal{F}(\boldsymbol{W},\vec{n})\, \mathrm{d}\sigma \simeq \Phi^R(W_i,W_j,\vec{\nu}_{ij})$$

where

$$\vec{\nu}_{ij} = \int_{\partial C_{ij}} \vec{n}\, \mathrm{d}\sigma$$

and W_k is the solution vector at the k-th node of the discretization. The numerical fluxes, Φ^R, are evaluated as follows:

$$\Phi^R(W_i,W_j,\vec{\nu}_{ij}) = \underbrace{\frac{\mathcal{F}(W_i,\vec{\nu}_{ij}) + \mathcal{F}(W_j,\vec{\nu}_{ij})}{2}}_{centered} - \underbrace{\gamma_s\, d^R(W_i,W_j,\vec{\nu}_{ij})}_{upwinding}$$

where $\gamma_s \in [0,1]$ is a parameter which directly controls the upwinding of the scheme and

$$d^R(W_i,W_j,\vec{\nu}_{ij}) = \left| \mathcal{R}(W_i,W_j,\vec{\nu}_{ij}) \right| \frac{W_j - W_i}{2}\ . \tag{2.7}$$

$\mathcal{R}$ is the Roe matrix and is defined as:

$$\mathcal{R}(W_i,W_j,\vec{\nu}_{ij}) = \frac{\partial \mathcal{F}}{\partial \boldsymbol{W}}(\widehat{\boldsymbol{W}},\nu_{ij}) \tag{2.8}$$

where $\widehat{\boldsymbol{W}}$ is the Roe average between W_i and W_j.

The classical Roe scheme is obtained as a particular case by imposing $\gamma_s = 1$. The accuracy of this scheme is only $1st$ order. In order to increase the order of accuracy of the scheme the MUSCL (*Monotone Upwind Schemes for Conservation Laws*) reconstruction method, introduced by Van Leer, Ref. [41], is employed. This method expresses the Roe flux as a function of the extrapolated values of $\boldsymbol{W}$ at the interface between the two cells C_i and C_j, W_{ij} and W_{ji}:

$$\int_{\partial C_{ij}} \mathcal{F}(\boldsymbol{W},\vec{n}) \, \mathrm{d}\sigma \simeq \Phi^R(W_{ij},W_{ji},\vec{\nu}_{ij})$$

where W_{ij} and W_{ji} are defined as follows:

$$W_{ij} = W_i + \frac{1}{2}(\vec{\nabla}\boldsymbol{W})_{ij} \cdot \vec{ij} \ , \tag{2.9}$$

$$W_{ji} = W_j + \frac{1}{2}(\vec{\nabla}\boldsymbol{W})_{ji} \cdot \vec{ij} \ . \tag{2.10}$$

To estimate the gradients $(\vec{\nabla}\boldsymbol{W})_{ij} \cdot \vec{ij}$ and $(\vec{\nabla}\boldsymbol{W})_{ji} \cdot \vec{ij}$ the $V6$ scheme is used, Ref. [7]:

$$
\begin{aligned}
(\vec{\nabla}\boldsymbol{W})_{ij} \cdot \vec{ij} =\ & (1-\beta)(\vec{\nabla}\boldsymbol{W})_{ij}^C \cdot \vec{ij}) + \beta(\vec{\nabla}\boldsymbol{W})_{ij}^U \cdot \vec{ij}) + \\
& \xi_c \, [(\vec{\nabla}\boldsymbol{W})_{ij}^U \cdot \vec{ij}) - 2(\vec{\nabla}\boldsymbol{W})_{ij}^C \cdot \vec{ij}) + (\vec{\nabla}\boldsymbol{W})_{ij}^D \cdot \vec{ij})] + \\
& \xi_c \, [(\vec{\nabla}W)_M \cdot \vec{ij}) - 2(\vec{\nabla}W)_i \cdot \vec{ij}) + (\vec{\nabla}W)_j^D \cdot \vec{ij})] \ , \tag{2.11}
\end{aligned}
$$

$$
\begin{aligned}
(\vec{\nabla}\boldsymbol{W})_{ji} \cdot \vec{ji} =\ & (1-\beta)(\vec{\nabla}\boldsymbol{W})_{ji}^C \cdot \vec{ij}) + \beta(\vec{\nabla}\boldsymbol{W})_{ji}^U \cdot \vec{ij}) + \\
& \xi_c \, [(\vec{\nabla}\boldsymbol{W})_{ji}^U \cdot \vec{ij}) - 2(\vec{\nabla}\boldsymbol{W})_{ji}^C \cdot \vec{ij}) + (\vec{\nabla}\boldsymbol{W})_{ji}^D \cdot \vec{ij})] + \\
& \xi_c \, [(\vec{\nabla}\boldsymbol{W})_{M'} \cdot \vec{ij}) - 2(\vec{\nabla}\boldsymbol{W})_i \cdot \vec{ij}) + (\vec{\nabla}\boldsymbol{W})_j^D \cdot \vec{ij})] \tag{2.12}
\end{aligned}
$$

where $(\vec{\nabla}\boldsymbol{W})_i$ and $(\vec{\nabla}\boldsymbol{W})_j$ are the nodal gradients at the nodes i and j respectively and are calculated as the average of the gradient on the tetrahedra $T \in C_i$, having the node i as a vertex. For example for $(\vec{\nabla}\boldsymbol{W})_i$ we can write:

$$(\vec{\nabla}\boldsymbol{W})_i = \frac{1}{Vol(C_i)} \sum_{T \in C_i} \frac{Vol(T)}{3} \sum_{k \in T} W_k \vec{\nabla}\Phi^{(i,T)} \ . \tag{2.13}$$

where $\Phi^{(i,T)}$ is the P1 finite-element basis function defined before. $(\vec{\nabla}\boldsymbol{W})_M \cdot \vec{ij}$, for the 3D case, is the gradient at the point M in Fig. 2.2 and it is computed by interpolation of the nodal gradient values at the nodes contained in the face opposite to the upwind tetrahedron T_{ij}. $(\vec{\nabla}\boldsymbol{W})_{M'} \cdot \vec{ij}$ is the gradient at the point M' in Fig. 2.2 and it is evaluated in the same way as $(\vec{\nabla}\boldsymbol{W})_M \cdot \vec{ij}$. The coefficients β, ξ_c, ξ_d are parameters that control the combination of fully upwind and centered slopes. The V6 scheme is obtained by choosing them to have the best accuracy on cartesian meshes, Ref.[7]:

$$\beta = 1/3, \qquad \xi_c - 1/30, \qquad \xi_d = -2/15 \ .$$
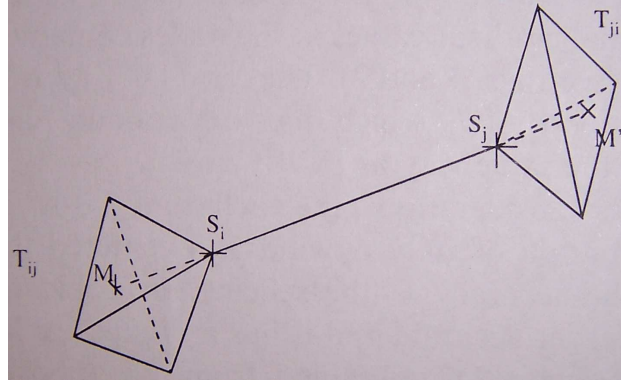
Figure 2.2.   Sketch of points and elements involved in the computation of gradient

Diffusive fluxes

The P1 finite-element basis function, $\phi^{(i,T)}$, restricted to the tetrahedron T is assumed to be of unit value on the node i and to vanish linearly at the remaining vertices of T. The Galerkin formulation for the diffusive terms is obtained by multiplying the diffusive terms by $\phi^{(i,T)}$ and integrating over the domain Ω_h:

$$\iint_{\Omega_h} \left(\frac{\partial V_j}{\partial x_j}\right) \phi^{(i,T)} \, \mathrm{d}\Omega = \iint_T \frac{\partial V_j}{\partial x_j} \phi^{(i,T)} \, \mathrm{d}\Omega \ .$$

Integrating by parts the right-hand side of Eq.(2.3) we obtain:

$$\iint_T \frac{\partial V_j}{\partial x_j} \phi^{(i,T)} \, \mathrm{d}\Omega = \iint_T \frac{\partial (V_j \phi^{(i,T)})}{\partial x_j} \, \mathrm{d}\Omega - \iint_T V_j \frac{\partial \phi^{(i,T)}}{\partial x_j} \, \mathrm{d}\Omega =$$
$$\int_{\partial T} V_j \phi^{(i,T)} n_j \, \mathrm{d}\sigma - \iint_T V_j \frac{\partial \phi^{(i,T)}}{\partial x_j} \, \mathrm{d}\Omega \ . \qquad (2.14)$$

In order to build the fluxes for the node i consistently with the finite-volume formulation, the contribution of all the elements having i as a vertex needs to be summed together as follows:

$$\sum_{T,i \, \in \, T} \left(\int_{\partial T} V_j \phi^{(i,T)} n_j \, \mathrm{d}\sigma - \iint_T V_j \frac{\partial \phi^{(i,T)}}{\partial x_j} \, \mathrm{d}\Omega \right) =$$
$$-\sum_{T,i \, \in \, T} \iint_T V_j \frac{\partial \phi^{(i,T)}}{\partial x_j} \, \mathrm{d}\Omega + \int_{\Gamma_h = \partial \Omega_h} \phi^{(i,T)} V_j n_j \, \mathrm{d}\sigma \ . \qquad (2.15)$$

In the P1 formulation for the finite-element method, the test functions, $\phi^{(i,T)}$, are linear functions on the element T and so their gradient is constant. Moreover, in the variational formulation the unknown variables contained in $\boldsymbol{W}$ are also approximated by their projection on the P1 basis function. For these reasons the integral can be evaluated directly.

2.4 Variational Multiscale approach (VMS)

For the New Hybriid Model the variational multiscale approach (VMS) is recovered in the LES mode. In this approach the flow variables are decomposed as follows:

$$w_i = \underbrace{\overline{w}_i}_{LRS} + \underbrace{w'_i}_{SRS} + w_i^{SGS} \qquad (2.16)$$

where $\overline{w}_i$ are the large resolved scales (LRS), w'_i are the small resolved scales (SRS). This decomposition is obtained by variational projection in the LRS and SRS spaces respectively. In the present study, we follow the VMS approach proposed in Ref.[18] for the simulation of compressible turbulent flows through a finite volume/finite element discretization on unstructured tetrahedral grids. If ψ_l are the N finite-volume basis functions and ϕ_l the N finite-element basis functions associated to the used grid, previously defined in Sec.2.3, in order to obtain the VMS flow decomposition in Eq. (2.16), the finite dimensional spaces $\mathcal{V}_{FV}$ and $\mathcal{V}_{FE}$, respectively spanned by ψ_l and ϕ_l, can be in turn decomposed as follows [18]:

$$\mathcal{V}_{FV} = \overline{\mathcal{V}}_{FV} \bigoplus \mathcal{V}'_{FV} \; ; \quad \mathcal{V}_{FE} = \overline{\mathcal{V}}_{FE} \bigoplus \mathcal{V}'_{FE} \qquad (2.17)$$

in which $\bigoplus$ denotes the direct sum and $\overline{\mathcal{V}}_{FV}$ and $\mathcal{V}'_{FV}$ are the finite volume spaces associated to the largest and smallest resolved scales, spanned by the basis functions $\overline{\psi_l}$ and ψ'_l; $\overline{\mathcal{V}}_{FE}$ and $\mathcal{V}'_{FE}$ are the finite element analogous. In Ref.[18] a projector operator P in the LRS space is defined by spatial average on macro cells in the following way:

$$\overline{\boldsymbol{W}} = P(\boldsymbol{W}) = \sum_k \underbrace{\left(\frac{Vol(C_k)}{\sum\limits_{j \epsilon I_k} Vol(C_j)} \sum_{j \epsilon I_k} \psi_j \right)}_{\overline{\psi}_k} \boldsymbol{W}_k \qquad (2.18)$$

for the convective terms, discretized by finite volumes, and:

$$\overline{\boldsymbol{W}} = P(\boldsymbol{W}) = \sum_k \underbrace{\left(\frac{Vol(C_k)}{\sum\limits_{j \epsilon I_k} Vol(C_j)} \sum_{j \epsilon I_k} \phi_j \right)}_{\overline{\phi}_k} \boldsymbol{W}_k \qquad (2.19)$$

for the diffusive terms, discretized by finite elements. In both Eqs. (2.18) and (2.19), $I_k = \{j/C_j \in C_{m(k)}\}$, $C_{m(k)}$ being the macro-cell containing the cell C_k. The macro-cells are obtained by a process known as agglomeration

[23]. The basis functions for the SRS space are clearly obtained as follows: $\psi'_l = \psi_l - \overline{\psi}_l$ and $\phi'_l = \phi_l - \overline{\phi}_l$. Finally, in the VMS approach the SGS model is added only to the smallest resolved scales. As in [18], the Smagorinsky model is used, and, hence, the SGS terms are discretized analogously to the viscous fluxes.

2.5 Discretization of the New Hybrid Model equations

Following the discretiazation and the assumptions introduced in the previous sections, the Galerkin projection of Eq. (1.50) becomes:

$$
\begin{aligned}
&\left(\frac{\partial \langle \boldsymbol{W} \rangle + \boldsymbol{W}^c}{\partial t}, \psi_l\right) + (\nabla \cdot F(\langle \boldsymbol{W} \rangle + \boldsymbol{W}^c), \psi_l) + \\
&(\nabla \cdot V(\langle \boldsymbol{W} \rangle + \boldsymbol{W}^c), \phi_l) = - \left(\tau^{LES}(\boldsymbol{W}'), \phi'_l\right) \quad l = 1, N
\end{aligned}
\tag{2.20}
$$

in which τ_{LES} is modeled by introducing a SGS eddy-viscosity μ_s, defined as in Eq.(1.33). Finally, the Galerkin projection of Eqs. (1.49) and (1.52) for the computation of $\langle \boldsymbol{W} \rangle$ and of the additional fluctuations in the proposed hybrid model become respectively:

$$
\begin{aligned}
&\left(\frac{\partial \langle \boldsymbol{W} \rangle}{\partial t}, \psi_l\right) + (\nabla \cdot F(\langle \boldsymbol{W} \rangle), \psi_l) + (\nabla \cdot V(\langle \boldsymbol{W} \rangle), \phi_l) = \\
&- \left(\tau^{RANS}(\langle \boldsymbol{W} \rangle), \phi_l\right) \quad l = 1, N
\end{aligned}
\tag{2.21}
$$

$$
\begin{aligned}
&\left(\frac{\partial \boldsymbol{W}^c}{\partial t}, \psi_l\right) + (\nabla \cdot F(\langle \boldsymbol{W} \rangle + \boldsymbol{W}^c), \psi_l) - (\nabla \cdot F(\langle \boldsymbol{W} \rangle), \psi_l) + \\
&(\nabla \cdot V(\boldsymbol{W}^c), \phi_l) = (1 - \theta) \left[\left(\tau^{RANS}(\langle \boldsymbol{W} \rangle), \phi_l\right) - \left(\tau^{LES}(\boldsymbol{W}'), \phi'_l\right)\right] \quad l = 1, N
\end{aligned}
\tag{2.22}
$$

2.5.1 Simplified model

To avoid the solution of two different systems of PDE and the consequent increase of required computational resources, Eqs. (2.21) and (2.22) can be recast together as follows:

$$
\begin{aligned}
&\left(\frac{\partial \boldsymbol{W}}{\partial t},\psi_l\right) + (\nabla \cdot F(\boldsymbol{W}),\psi_l) + (\nabla \cdot V(\boldsymbol{W}),\phi_l) = \\
&-\theta\left(\tau^{RANS}(\langle\boldsymbol{W}\rangle),\phi_l\right) - (1-\theta)\left(\tau^{LES}(\boldsymbol{W}'),\phi_l'\right) \quad l = 1,N
\end{aligned}
\tag{2.23}
$$

Clearly, if only Eq. (2.23) is solved, $\langle\boldsymbol{W}\rangle$ is not available at each time step. Two different options are possible: either to use an approximation of $\langle\boldsymbol{W}\rangle$ obtained by averaging and smoothing of $\boldsymbol{W}$, in the spirit of VMS, or to simply use in Eq. (2.23) $\tau^{RANS}(\boldsymbol{W})$. The second option is adopted in the present study as a first approximation.

2.6 Boundary conditions

Firstly, the real boundary Γ is approximated by a polygonal boundary Γ_h that can be split in two parts:

$$
\Gamma_h = \Gamma_\infty + \Gamma_b
\tag{2.24}
$$

where the term Γ_∞ represents the far-fields boundary and Γ_b represents the body surface. The boundary conditions are set using the Steger-Warming formulation ([39]) on Γ_∞ and using slip or no-slip conditions on Γ_b.

In the AERO code a wall-law method (Reichardt wall-law) is used to set the no-slip boundary conditions. The boundary treatment is controlled by the parameter δ, which sets the distance from the wall at which slip conditions are imposed. The velocity is assumed to vanish at the wall, starting by the value computed at the distance δ, by following the Reichardt wall-law. Appropriate values of the shear stress are obtained from the friction velocity (u_τ) computed as:

$$\frac{\bar{u}}{u_\tau} = \frac{1}{k} ln(1 + kz^+) + 7.8 \left(1 - e^{\frac{z^+}{11}} - \frac{z^+}{11} e^{-0.33 z^+} \right). \qquad (2.25)$$

and used in the simulations as boundary condition. This law has the advantage of describing the velocity profile not only in the logarithmic region of a boundary layer but also in the laminar sublayer and in the intermediate region.

2.7 Time advancing

Once the equations have been discretized in space, the unknown of the problem is the solution vector at each node of the discretization as a function of time, $\boldsymbol{W}_h(t)$. Consequently the spatial discretization leads to a set of ordinary differential equations in time:

$$\frac{d\boldsymbol{W}_h}{dt} + \Psi(\boldsymbol{W}_h) = 0 \qquad (2.26)$$

where Ψ_i is the total flux, containing both convective and diffusive terms, of W_h through the i-th cell boundary divided by the volume of the cell.

Explicit time advancing

In the explicit case a N-step low-stockage Runge-Kutta algorithm is used for the discretization of Eq.(2.26):

$$\begin{cases} \boldsymbol{W}^{(0)} = \boldsymbol{W}^{(n)}, \\ \boldsymbol{W}^{(k)} = \boldsymbol{W}^{(0)} + \Delta t \; \alpha_k \; \Psi(\boldsymbol{W}^{(k-1)}), \quad k = 1,\dots ,N \\ \boldsymbol{W}^{(n+1)} = \boldsymbol{W}^{(N)}. \end{cases}$$

in which the subfix h has been omitted for sake of simplicity. Different schemes can be obtained varying the number of steps, N, and the coefficients α_k.

Implicit time advancing

For the implicit time advancing scheme in AERO the following second order accurate backward difference scheme is used:

$$\alpha_{n+1}\boldsymbol{W}^{(n+1)} + \alpha_n\boldsymbol{W}^{(n)} + \alpha_{(n-1)}\boldsymbol{W}^{(n-1)} + \Delta t^{(n)}\Psi(\boldsymbol{W}^{(n+1)}) = 0 \qquad (2.27)$$

where the coefficients α_n can be expressed as follows:

$$\alpha_{n+1} = \frac{1 + 2\tau}{1 + \tau}, \qquad \alpha_n = -1 - \tau, \qquad \alpha_{n-1} = \frac{\tau^2}{1 + \tau} \qquad (2.28)$$

where $\Delta t^{(n)}$ is the time step used at the n-th time iteration and

$$\tau = \frac{\Delta t^{(n)}}{\Delta t^{(n-1)}}. \qquad (2.29)$$

The nonlinear system obtained can be linearized as follows:

$$\alpha_{n+1}\boldsymbol{W}^{(n)} + \alpha_n\boldsymbol{W}^{(n)} + \alpha_{(n-1)}\boldsymbol{W}^{(n-1)} + \Delta t^{(n)}\Psi(\boldsymbol{W}^{(n)}) =$$
$$-\left[\alpha_{n+1} + \delta t^{(n)}\frac{\partial \Psi}{\partial \boldsymbol{W}}(\boldsymbol{W}^{(n)})\right](\boldsymbol{W}^{(n+1)} - \boldsymbol{W}^{(n)}). \qquad (2.30)$$

Following the deflect-correction approach, the jacobians are evaluated using the 1st order flux scheme (for the convective part), while the explicit fluxes are composed with 2nd order accuracy. The resulting linear system is iteratively solved by Jacobi relaxation.

Chapter 3

Flow around a square cylinder

3.1 Description of the test case and of the simulation parameters

The flow around a square cylinder of infinite spanwise length is considered. The Reynolds number, based on the cylinder side length and on the freestream velocity, is equal to 22000 and the used computational domain is represented in Fig. 3.1, together with the frame of reference.

With reference to Fig. 3.1, the domain dimensions are the following: $L_i/D = 4.5$, $L_o/D = 9.5$, $H_y/D = 7$, $H_z/D = 9.75$. They are equal to those employed in the LNS simulations in [8].

The computational domain in Fig. 3.1 is discretized by generating two unstructured grids made of tetrahedral elements (grid GR1 and GR2 in Tab. 3.1). The two grids have a different resolution in order to test the influence of this parameter on the model. The section $z = 0$ of the first grid and $z = 4.875$ of the second are reported in Fig. 3.2(a),(b).

Approximate boundary conditions, based on the Reichardt wall-law [15] [28], are applied at the solid walls (see Sec.2.6). This type of wall treatment has been succesfully used in previous LES ([6], [7], [18]), RANS ([28], [29]) and LNS ([8]) simulations of the same flow. This approach allows the same

boundary conditions to be used for both the RANS closure and the LES Smagorinsky model. At the inflow, the flow is assumed to be undisturbed and the Steger-Warming [39] conditions are applied. Boundary conditions based on the Steger-Warming decomposition are used at the outflow as well. On the other surfaces ($y = \pm H_y$, $z = \pm H_z$) slip conditions are imposed.
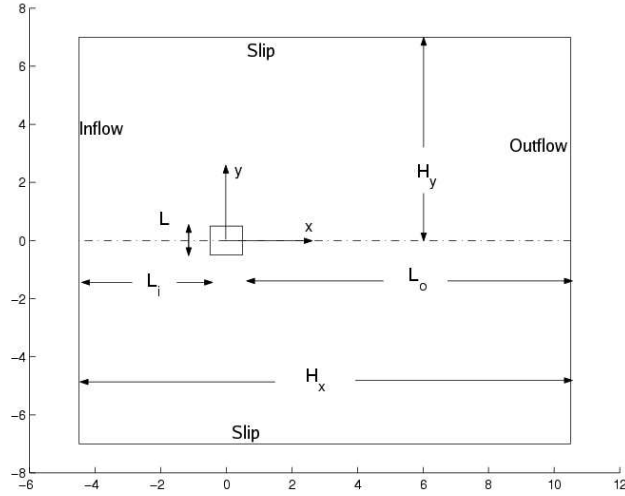
Figure 3.1. Computational domain (side view)
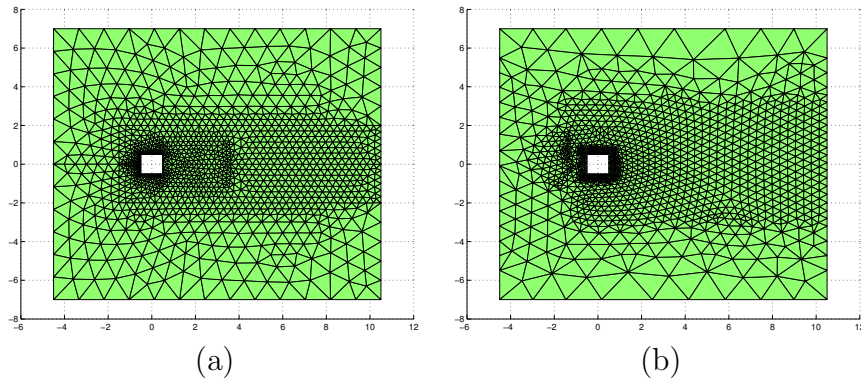
Figure 3.2. Section at $z = 0$ of grid GR1(a) and section at $z = 4.875$ of GR2 (b)

For both grids, the computations have been carried out using the LNS model and the new proposed hybrid model with the three different definitions of the blending parameter.

	N. nodes	N. elements
Gr1	8.3×10^4	4.75×10^5
Gr2	3.5×10^4	1.9×10^5

Table 3.1.   Main feature of the computational domains and grids

The simulations have been carried out with different values of k_0 (the inflow value of k for the RANS model) and δ (the parameter of the wall-law) to test the sensitivity of the model to these features.

Following the LNS work in [8], the numerical parameter γ, which controls the amount of numerical viscosity introduced in the simulation, has been set equal to 0.1 for GR1 and 0.5 for GR2, in order to obtain stable simulations.

The simulations have been implicitly advanced in time, with a maximum CFL number in the range from 10 to 20. In a previous work ([8]), it was shown that no significant information is lost in time provided that CFL$\leq$ 25.

The parameters caracterizing the different simulations are summarized in Tab. 3.2.

Simulations	Grid	δ	γ	CFL	Model	k_0
LNS2	Gr1	0.0041	0.1	10	LNS	$U_0/1000$
LNS3	Gr1	0.02	0.1	10	LNS	$U_0/1000$
LNS5	Gr2	0.02	0.5	10	LNS	$U_0/1000$
LNS6	Gr2	0.02	0.5	10	LNS	$U_0/10000$
BLE1	Gr1	0.0041	0.1	10	$\tanh((\nu_{VMS-LES}/\nu_{k-\varepsilon})^2)$	$U_0/1000$
BLE2	Gr1	0.02	0.1	10	$\tanh((\nu_{VMS-LES}/\nu_{k-\varepsilon})^2)$	$U_0/1000$
BLE4	Gr1	0.0041	0.1	20	$\tanh((t_{VMS-LES}/t_{k-\varepsilon})^2)$	$U_0/1000$
BLE5	Gr1	0.02	0.1	10	$\tanh((t_{VMS-LES}/t_{k-\varepsilon})^2)$	$U_0/1000$
BLE6	Gr2	0.06	0.5	10	$\tanh((\nu_{VMS-LES}/\nu_{k-\varepsilon})^2)$	$U_0/1000$
BLE7	Gr2	0.02	0.5	10	$\tanh((\nu_{VMS-LES}/\nu_{k-\varepsilon})^2)$	$U_0/1000$
BLE8	Gr2	0.02	0.5	10	$\tanh((\nu_{VMS-LES}/\nu_{k-\varepsilon})^2)$	$U_0/10000$
BLE9	Gr2	0.02	0.5	10	$\tanh((t_{VMS-LES}/t_{k-\varepsilon})^2)$	$U_0/1000$
BLE10	Gr2	0.02	0.5	10	$\tanh((t_{VMS-LES}/t_{k-\varepsilon})^2)$	$U_0/10000$
BLE11	Gr2	0.02	0.5	10	$\tanh((L_{VMS-LES}/L_{k-\varepsilon})^2)$	$U_0/1000$
BLE12	Gr2	0.02	0.5	10	$\tanh((L_{VMS-LES}/L_{k-\varepsilon})^2)$	$U_0/10000$

Table 3.2.   Simulation parameters

3.2   Analisys of the results

A brief summary of the global flow parameters obtained in the different simulations and of some experimental data can be found in Tab.3.3. In this table numerical results from DES simulations are also shown. In particular, the sensitivity to the hybridization model, to δ and to k_0 are investigated. For each of the considered cases, figures showing the iso-contours of the blending parameter and of the LES or RANS eddy viscosities are reported, in order to highligth the behavior of the different considered hybridization strategies. Some mean velocity profiles are also shown and compared to experimental data.

3.2.1   Model influence

The model influence was tested for both grids. For the grid GR1, it is possible to compare simulations BLE1 and BLE4, in which the blending parameter is based on the viscosity ratio (VR) and time ratio (TR) respectively, with the simulation LNS2, which employs the LNS model. Figure 3.3 and 3.4 show the blending parameter (a), the VMS-LES (c) and RANS (d) viscosity fields, for BLE1 and BLE4; in fig. 3.5 the viscosity fields (LES (a), RANS (b)) are plotted and also the isoline at LNS parameter $\alpha = 0.95$. This is a numerical threshold between the zones in which the LNS model works in LES or RANS mode. It is important to underline that LNS works only in RANS or in LES mode and thus it is possible to define a threshold value like that explained before. In the new proposed hybrid model this is not possible because the model can work also in an hybrid mode as shown in Sec.1.6. The simulation BLE1 seems to work in LES mode in the whole domain except near the wall of the cylinder in which the RANS model is adopted (fig.3.3(b)) and in some part outside of the wake (upwind from the cylinder, in the shear layers and near the lateral boundary) where the hybrid mode is setted. This is in accord with the viscosity fields, μ_s being lower than μ_t in the wake and comparable in those points of the field where the

model works in the hybrid mode. Looking at BLE4 the differences with respect to BLE1 are evident. In the wake the model works not only in LES mode but there are also hybrid and RANS zones, the zone using RANS in the shear layers is larger that previously and around the wall the RANS mode is only near the upwind corners. This configuration is not completely in accord with the viscosity fields because, for example, in the wake the VMS-LES viscosity is everywhere lower than the RANS one while the model works somewhere in RANS mode. Comparing the two simulations with the LNS it is possible to see that the behaviour of the LNS model in the wake and outside is similar to that of BLE1 but the zone around the cylinder is closer to that of BLE4. Looking at the numerical results, from Tab.3.3, it appears that in the LNS2 simulation a better prediction of the mean drag coefficient $\overline{C_d}$ is obtained than in BLE1 and BLE4. The rms values of lift and drag coefficient and of the Strouhal number obtained in the different simulations are very similar. The length of the recirculation bubble (l_r) is overestimated in all cases. Figure 3.6 shows the streamwise velocity profiles along the centerline (Fig. 3.6 (a)) and in the lateral direction at two different locations in the wake (x/h=1.25 in Fig. 3.6 (b) and x/h=2.5 in Fig. 3.6 (c)). It can be seen that the differences between the models are small. The overall agreement with the experiments may be considered satisfactory, except for the much higher recovery velocity obtained in all simulations with respect to the experiments. This is, however, a discrepancy observed in almost all the previous simulations in the literature and is dicussed, for instance, in [6].

Simulations BLE2 and BLE5 , using the same models as BLE1 and BLE4, but with a different δ, can be compared with LNS3.

Figure 3.7, 3.8 and 3.9 report the same quantities previously discussed for BLE1, BLE4, LNS2 and namely the blending parameter, the LES and RANS eddy-viscosity. It seems that the behaviour of the blending parameter is the same as that observed for the previous set of simulations except for the zone around the cylinder in BLE2 (3.7(b)), in which the model now works in the hybrid mode with only small RANS regions near the corner

of the cylinder (fig.3.7 (b)). The results, with reference to Tab.3.3, show that $\overline{C_d}$ is better predicted than previously in all the presently considered cases. As previously, the values of r.m.s. of the force coefficients and of the Strouhal number are very similar for the different simulations. The mean recirculation length obtained in BLE5 and LNS3 is the same and is lower than the experimental value. Coversely, the length obtained in BLE2 is very close to the experimental one. For the mean velocity profiles (shown in Fig. 3.10), the same considerations as previously can be made, except that in this case BLE2, i.e. the simulations employing the viscosity ratio as blending parameter, seems to give a better agreement with the experiments than the other models. It should also be underlined that the differences between LNS3 and BLE5 are very small.

For the grid GR2, the simulations BLE7, BLE9 and BLE11, using VR, TR, and the length ratio (LR) respectively as blending parameters, can be compared with the LNS simulation LNS5 or BLE8, BLE10 and BLE12, which employ the same models as BLE7, BLE9 and BLE11 respectively, but with a different k_0, can be compared with LNS6. The global parameters (Tab.3.3) are very similar for all the different versions of the new hybrid model, but it seems that LR gives a slightly better prediction of the r.m.s. values of the force coefficients and TR of the mean recirculation length. However, the r.m.s. values of the force coefficients are underestimated in all the simulations and the best agreement with the experiments is obtained with LNS. The mean drag coefficient is well predicted in all the simulations, the maximum error is less than 4%. As it is possible to see in fig. 3.11 (a) (BLE7), fig. 3.12 (b) (BLE9) and fig. 3.13 (c) (BLE11), the hybrid model based on TR and VR as blending parameters has a behaviour very similar to the one on grid GR1. In the other case (LR as blending parameter), into the wake the model works in VMS-LES mode. Starting from the upwind corner the wake is bounded by a RANS zone and then (most of all in the upwind part) there is a zone where the model works in an hybrid way. In the other part of the domain RANS mode is used. The velocity profiles, shown in Figs. 3.15 and 3.20, are also

for this case not very sensitive to the model and the overal agreement with the experiments is rather satisfactory (except for the recovery velocity in the far wake, as previously discussed), especially for the very coarse considered grid.

3.2.2 Sensitivity to the inflow value of the turbulent kinetic energy, k_0

The sensitivity to the inflow value of the turbulent kinetic energy, k_0, was tested only on grid GR2. The numerical predictions of the flow global parameters (compare BLE7 vs BLE8 or BLE9 vs BLE10 or BLE11 vs BLE12 in Tab.3.2) seem not to be very sensitive to this parameter. Also, the mean velocity profiles obtained with different values of k_0 are very similar, as can be noticed by comparing fig.3.15 with fig.3.20. The only visible change is in the blending function behaviour: it seems that decreasing the value of k_0 there is a larger region outside the wake in which the RANS model is used (compare for example fig.3.13(a) with fig.3.18(a)). This is due to the different value of the RANS viscosity in the inlet part of the domain, compare for example fig.3.13(d) with fig.3.18(d). Indeed, it is possible to see that the RANS viscosity in BLE11 shows a step decrease in the inlet part that is not present in BLE12. This seems to indicate that in BLE11 the inlet value of k_0 is too high. However, the fact that the results are not sensitive to k_0 indicates that the proposed hybridization strategies does not require a fine tuning of the inlet RANS parameters, which is conversely important in pure RANS calculations.

3.2.3 Sensitivity to the parameter δ in the approximate wall treatment

The sensitivity to the parameter δ in the approximate wall treatment (see Sec. 2.6) was tested only on grid GR1. As for the global parameters (compare

BLE1 with BLE2 or BLE4 with BLE5 in Tab.3.2), when δ is increased, the accuracy of the numerical prediction of $\overline{C_d}$, St and l_r seems to be improved, while that of the numerical prediction of the r.m.s. of the force coefficents seems to deteriorate. The blending parameter, as function of δ, changes its behaviour only in the zone near the cylinder: increasing δ the RANS zone decrease (compare fig. 3.3(a) with fig.3.7(a)). The mean velocity profiles are very sensitive to this parameter. The first comparison that can be made is between fig. 3.6(a) and fig. 3.10(a), which shows the x-component of the velocity (u) in the plane $y/L = 0$. Increasing δ the curves are traslated backward with respect to the x axis and the slope is increased. Then, it is possible to compare fig. 3.6(b) and fig. 3.10(b), showing the u profile in the plane $x/L = 1.5$. Increasing δ there is a traslation towards higher values near the middle of the wake ($y/L = 0$) and towards lower values outside (higher y). TR (BLE4 and BLE5) and LNS (LNS2 and LNS3), are subjected to larger variations than VR (BLE1 and BLE2). In addiction the behaviour of the profile of BLE1 and BLE2 seems closer to that of the experimental data. Looking at fig.3.6(c) and fig.3.10(c), in which the u profile of the plane $x/L = 2.5$ is reported, it can be seen that the results are also affected by δ. For example in the zone between $1 < y/L < 2.5$ the curves of the simulations with $\delta = 0.02$ are closer to the experimental data than those with $\delta = 0.0041$.
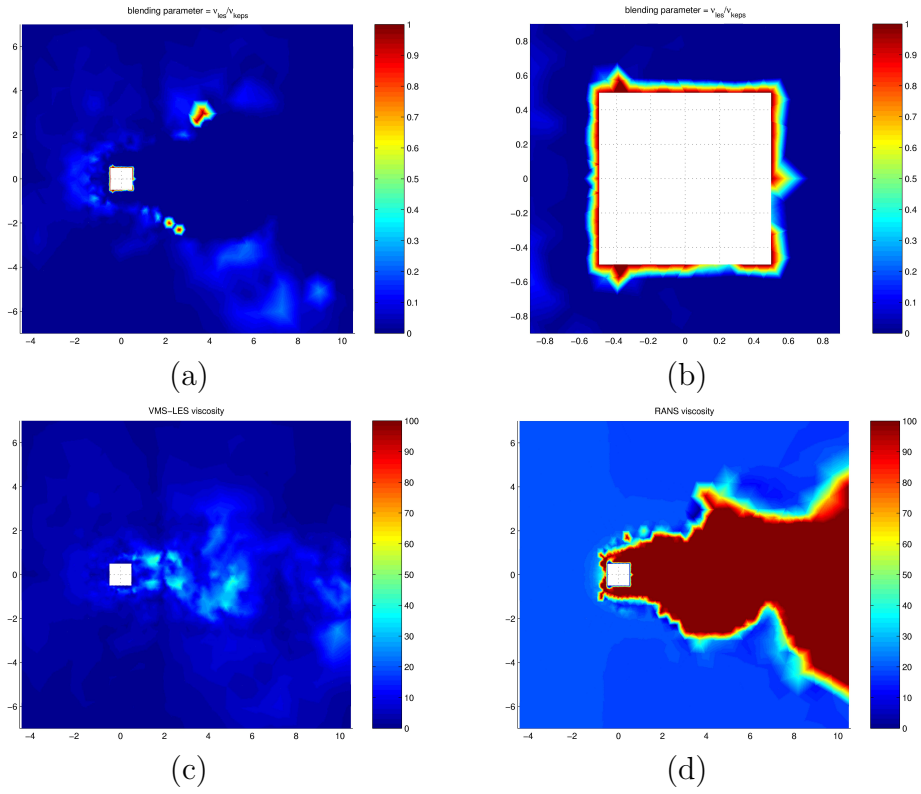
Figure 3.3.   Plot of the blending parameter (a) and zoom around the cylinder (b), plot of the VMS-LES viscosity (c) and RANS viscosity (d) for the BLE1 parameter.
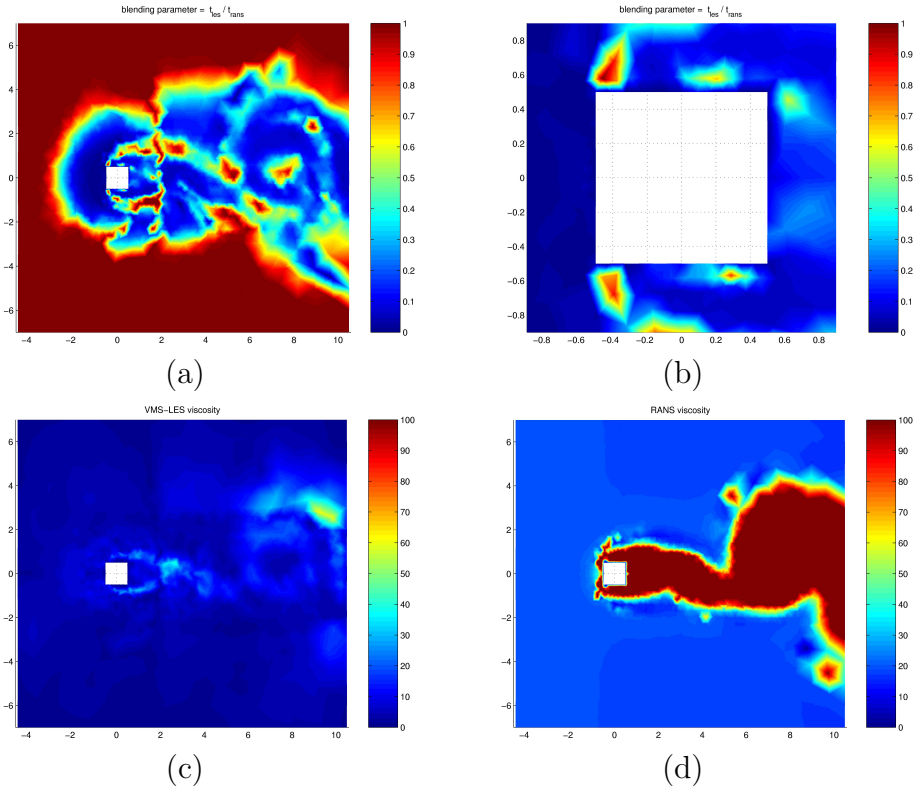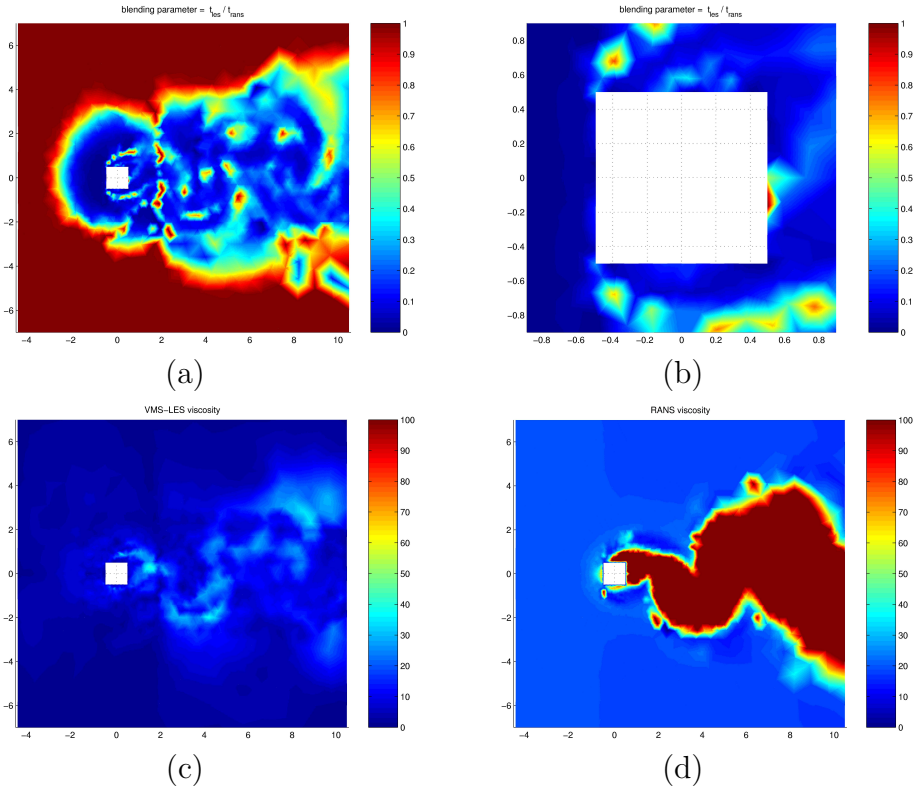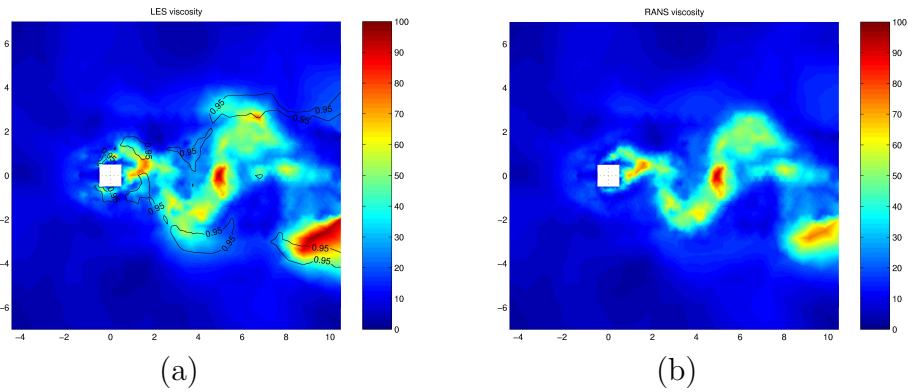
Figure 3.4.   Plot of the blending parameter (a) and zoom around the cylinder (b), plot of the VMS-LES viscosity (c) and RANS viscosity (d) for the BLE4 parameter.
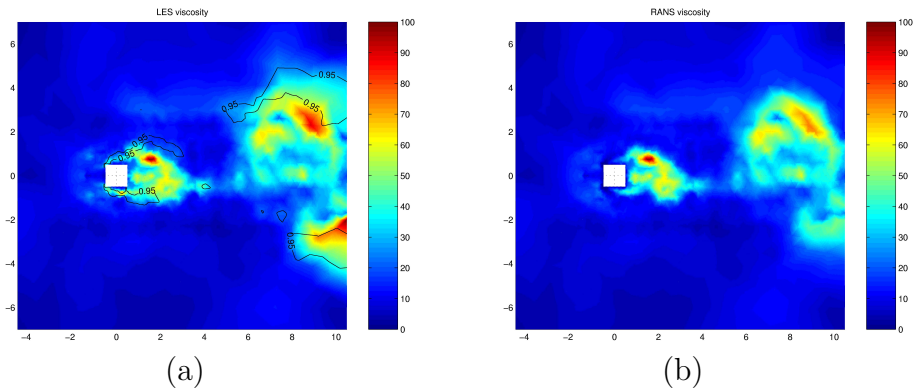
Figure 3.5.   Plot of the VMS-LES viscosity with isoline at LNS parameter=0.95 (a) and RANS viscosity (b) for the LNS2.
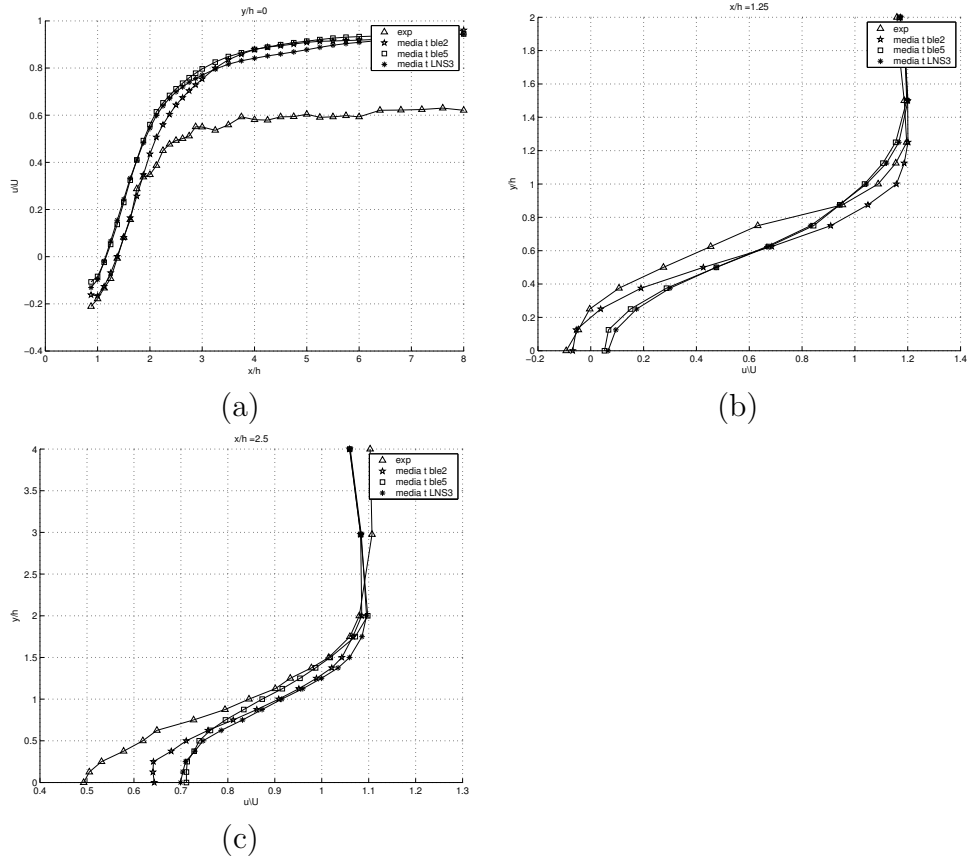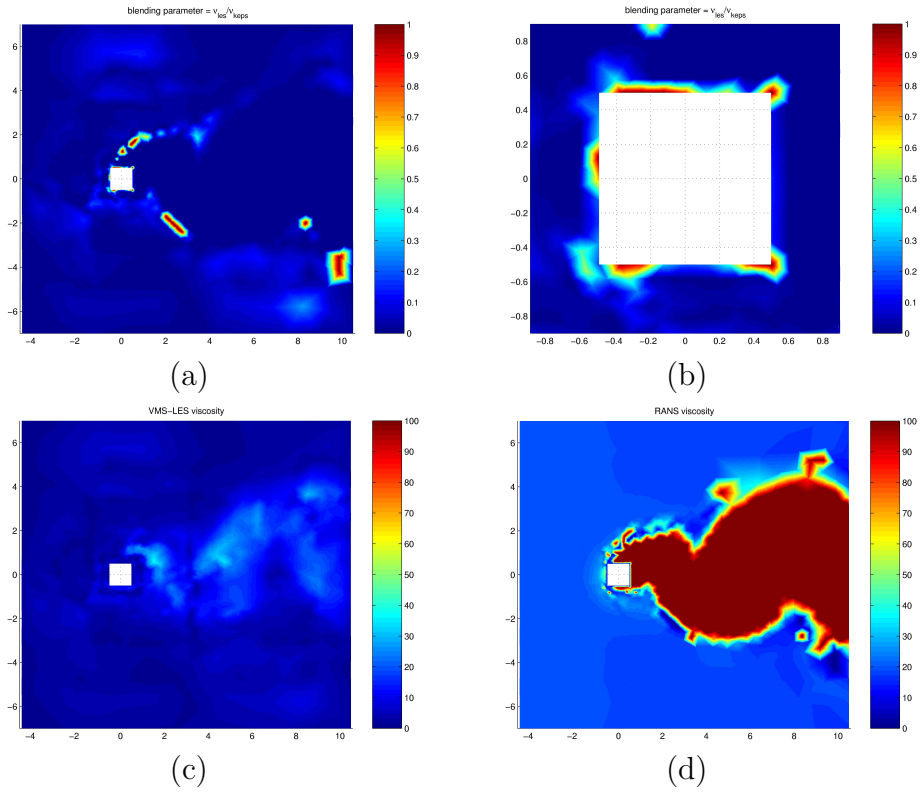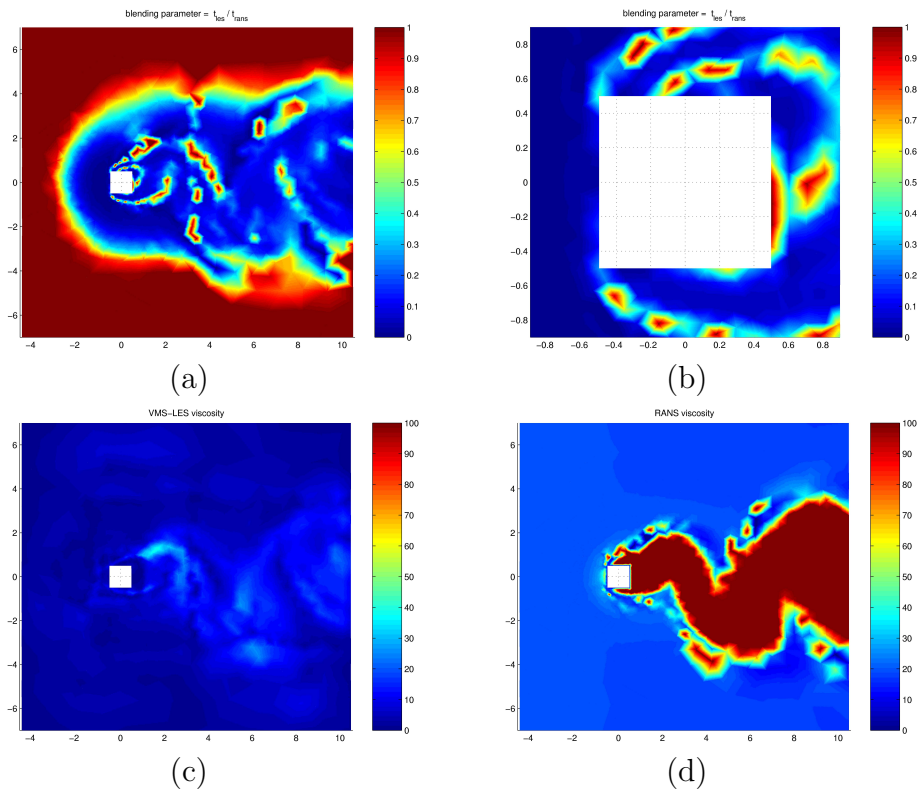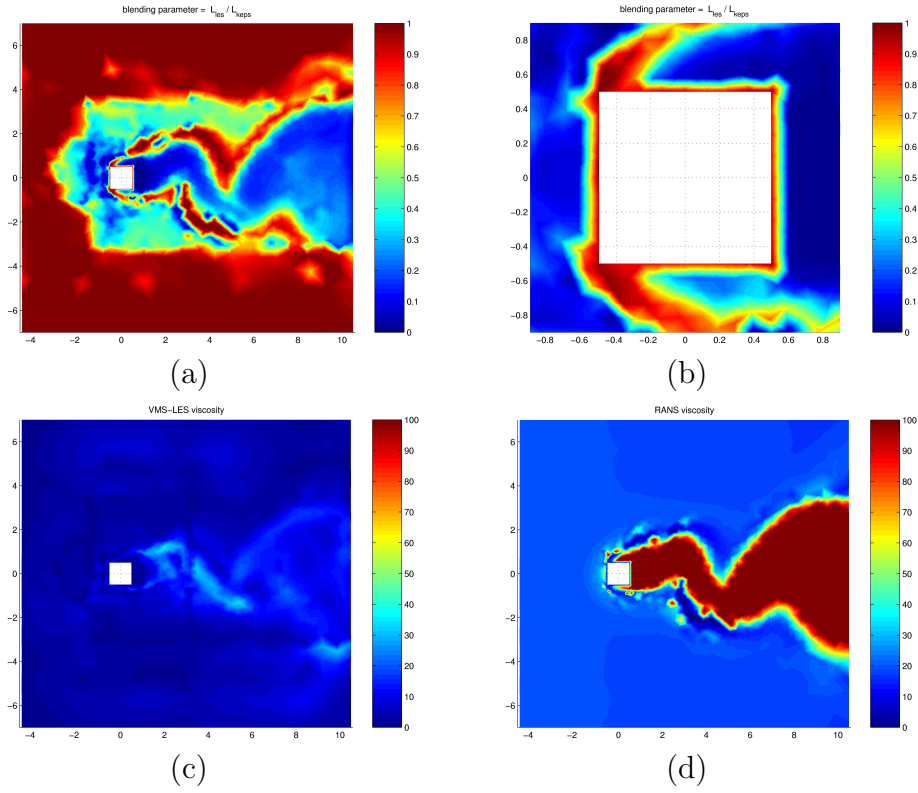
(a)

(b)

(c)
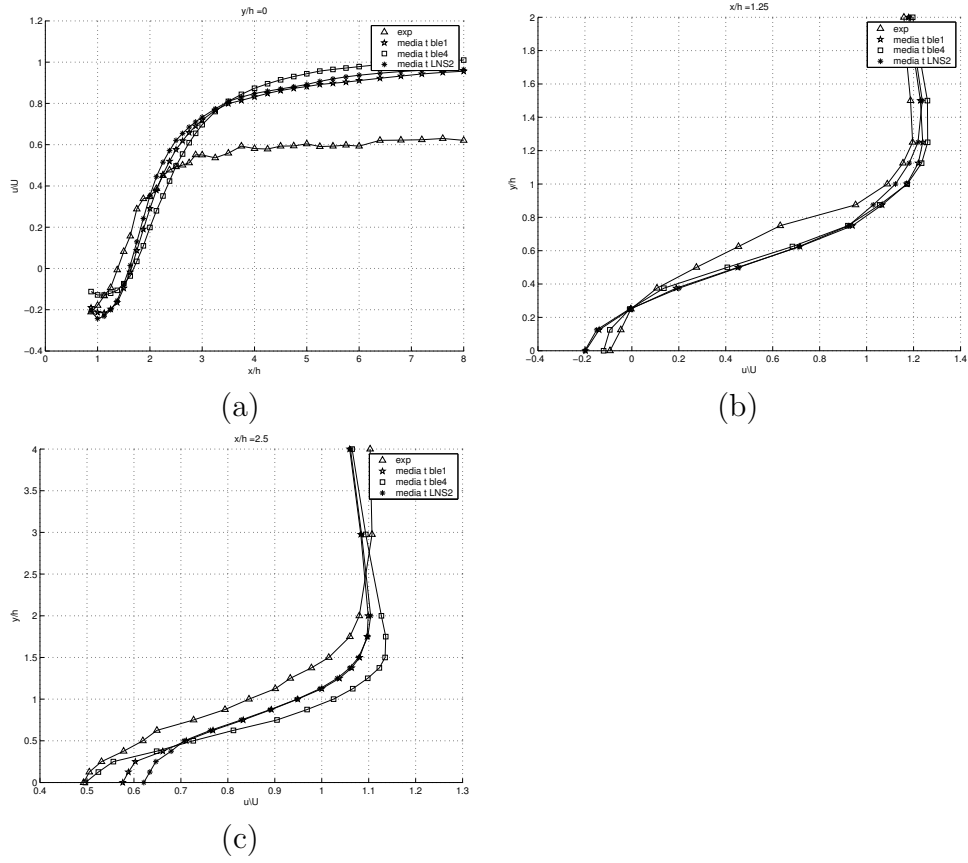
Figure 3.6.   u velocity profiles for BLE1, BLE4 and LNS2 plane y/L=0
(a), x/L=1.25 (b), x/L=2.5 (c)

47
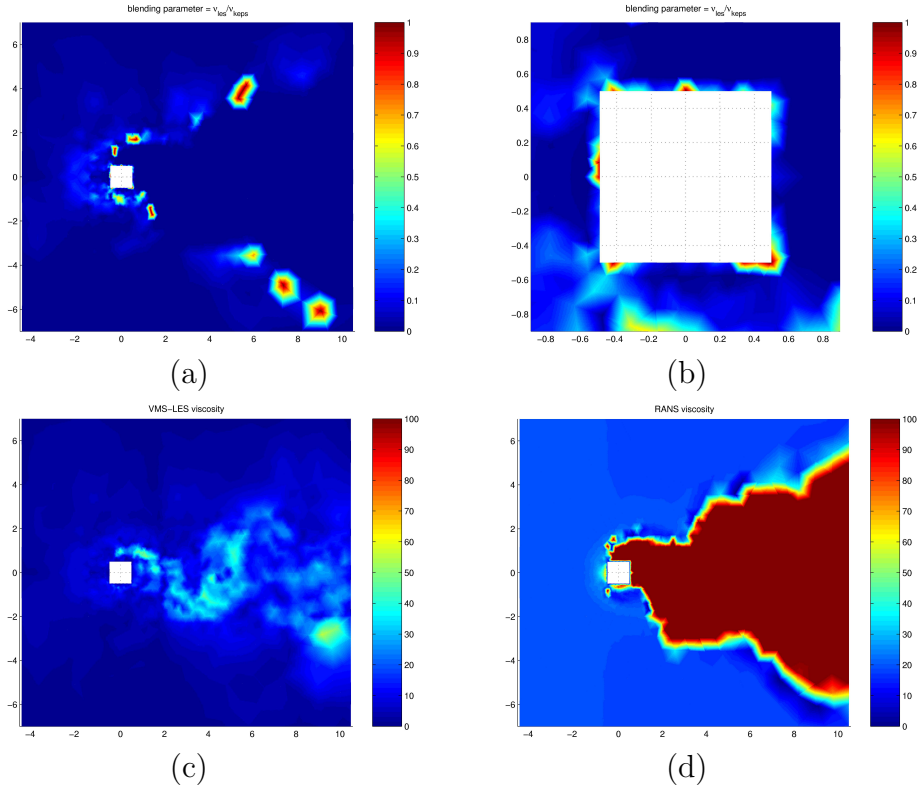
Figure 3.7.   Plot of the blending parameter (a) and zoom around the cylinder (b), plot of the VMS-LES viscosity (c) and RANS viscosity (d) for the BLE2 parameter.
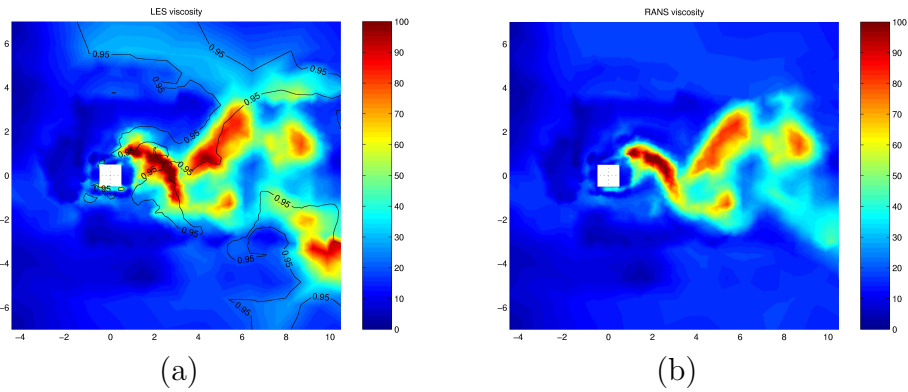
Figure 3.8.   Plot of the blending parameter (a) and zoom around the cylinder (b), plot of the VMS-LES viscosity (c) and RANS viscosity (d) for the BLE5 parameter.

Figure 3.9.   Plot of the VMS-LES viscosity with isoline at LNS parameter=0.95 (a) and RANS viscosity (b) for the LNS3.
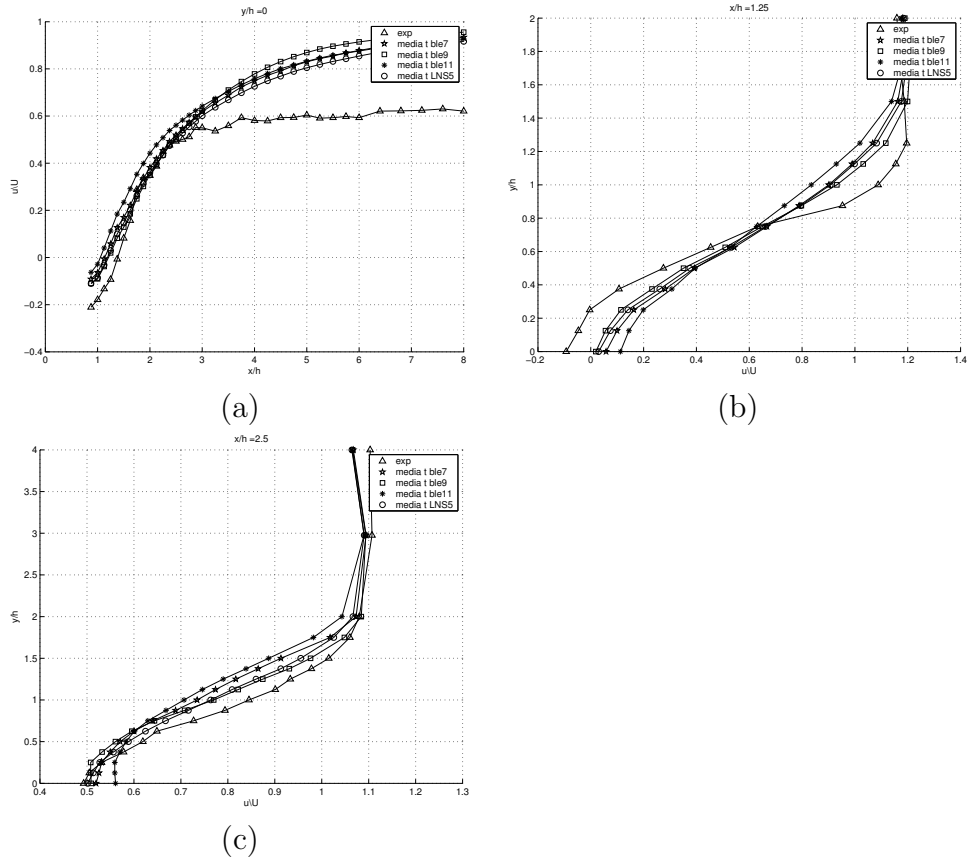
49

(a)

(b)

(c)

Figure 3.10.   u velocity profiles for BLE2, BLE5 and LNS3 plane y/L=0
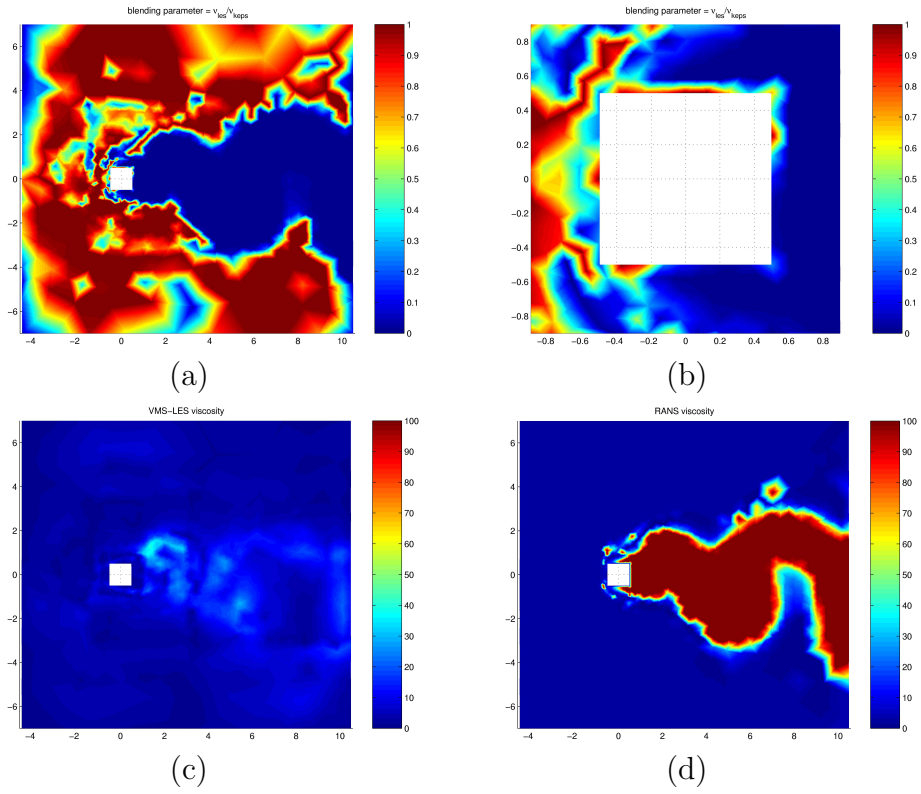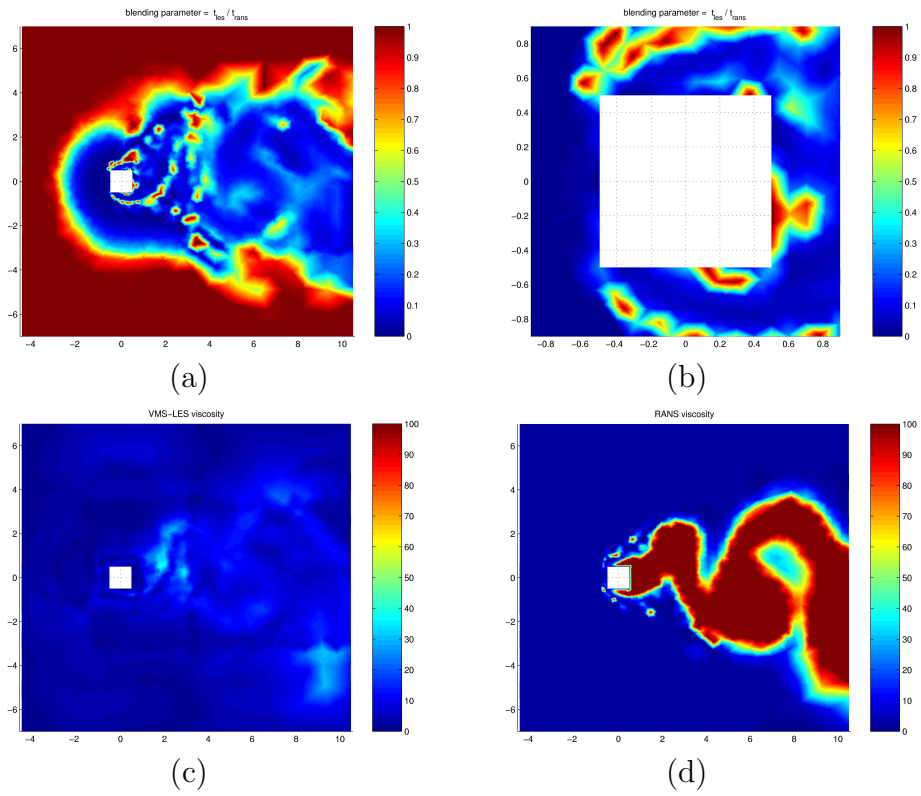(a), x/L=1.25 (b), x/L=2.5 (c)

Figure 3.11. Plot of the blending parameter (a) and zoom around the cylinder (b), plot of the VMS-LES viscosity (c) and RANS viscosity (d) for the BLE7 parameter.

Figure 3.12. Plot of the blending parameter (a) and zoom around the cylinder (b), plot of the VMS-LES viscosity (c) and RANS viscosity (d) for the BLE9 parameter.
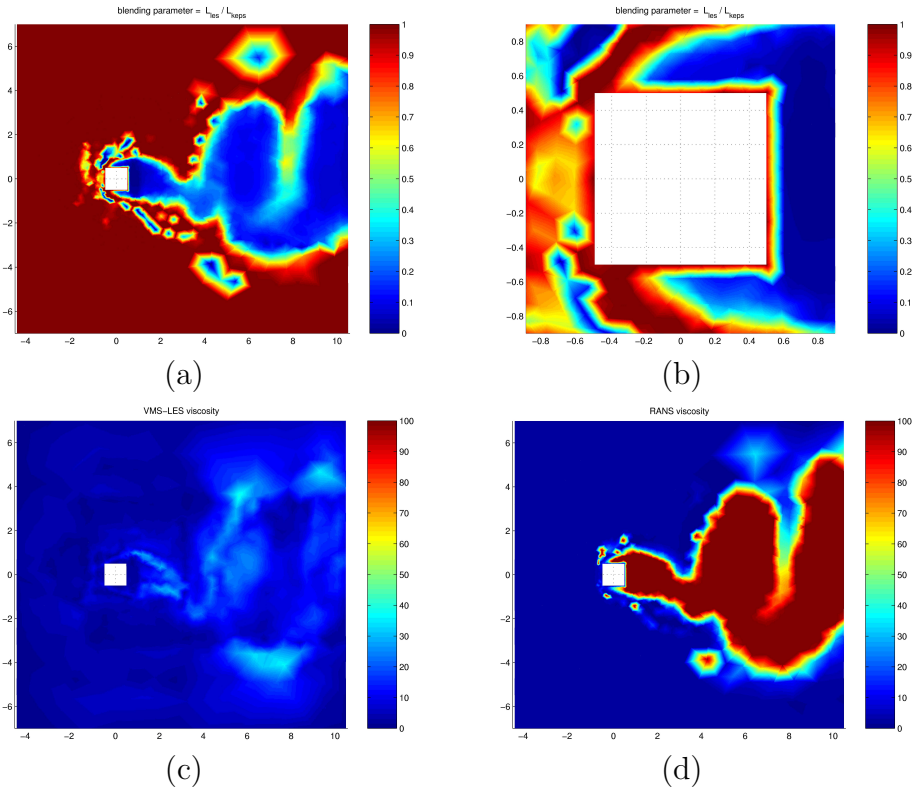
Figure 3.13.   Plot of the blending parameter (a) and zoom around the cylinder (b), plot of the VMS-LES viscosity (c) and RANS viscosity (d) for the BLE11 parameter.

Figure 3.14.   Plot of the VMS-LES viscosity with isoline at LNS parameter=0.95 (a) and RANS viscosity (b) for the LNS5.

(a)

(b)

(c)

Figure 3.15.   u velocity profiles for BLE7, BLE9, BLE11 and LNS5 plane
y/L=0 (a), x/L=1.25 (b), x/L=2.5 (c)

Figure 3.16. Plot of the blending parameter (a) and zoom around the cylinder (b), plot of the VMS-LES viscosity (c) and RANS viscosity (d) for the BLE8 parameter.

Figure 3.17. Plot of the blending parameter (a) and zoom around the cylinder (b), plot of the VMS-LES viscosity (c) and RANS viscosity (d) for the BLE10 parameter.
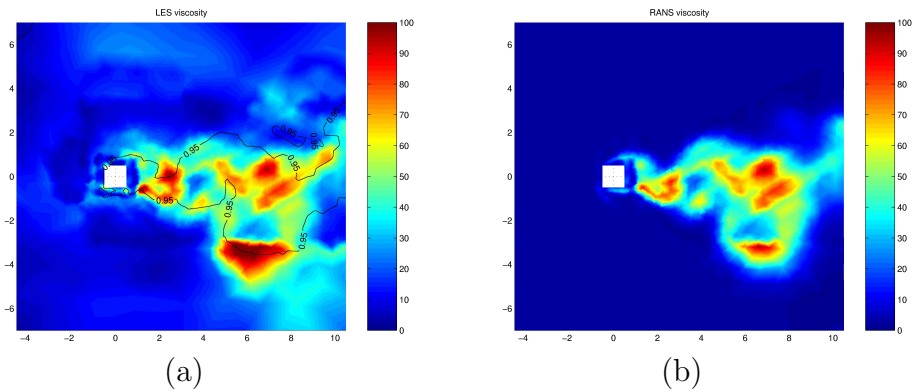
Figure 3.18. Plot of the blending parameter (a) and zoom around the cylinder (b), plot of the VMS-LES viscosity (c) and RANS viscosity (d) for the BLE12 parameter.

Figure 3.19. Plot of the VMS-LES viscosity with isoline at LNS parameter=0.95 (a) and RANS viscosity (b) for the LNS6.
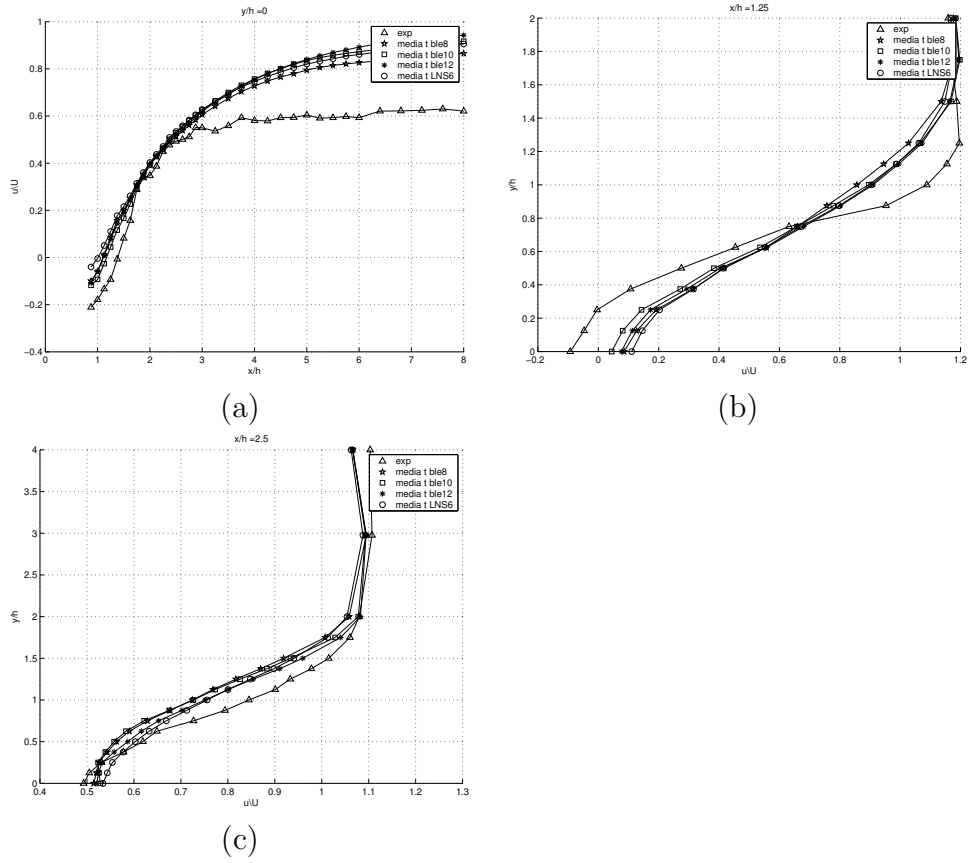
(a)

(b)

(c)

Figure 3.20.   u velocity profiles for BLE8, BLE10, BLE12, LNS6 plane
y/L=0 (a), x/L=1.25 (b), x/L=2.5 (c)

3.2.4   Comparison with DES simulations

The numerical results obtained with the LNS and the new hybrid model are compared with those obtained with DES by *Schmidt et al.* (DES1) (Ref.[35]) and by *Lo et al.* (DES2) (Ref.[25]). DES1 has been carried out on the same domain used in our simulations. A structured grid with 32 thousand nodes for each transversal plane has been used to discretized the domain. This grid is more refined than that used in our simulation, which has one thousand nodes in the middle plane. Moreover, the distance of the first mesh points to the cylinder wall is two order of magnitude smaller than that used in our simulations. The used flow solver in Ref.[35] is based on an implicit pressure-based finite volume Navier-Stokes procedure applying a cell-centred discretisation on semi-structured grids. The code is second-order accurate in space and time and uses multi-block algorithms. The results from DES2 are computed on a larger domain (the length of the domain behind the cylinder is twice that used in our simulations) and a finer grid (having 500000 nodes). For this simulation a commercial code has been used used. This is a cell-centred, finite volume, unstructured compressible flow solver (more informations about this code can be found in Ref.[9]).

With reference to Tab.3.3 it is possible to appreciate as DES gives higher values of the $\overline{C_d}$ with respect to all the simulations carried out with the LNS and the new hybrid model. Particularly, DES2 gives the best value comparing with the experiments. Looking at the rms values, DES seems to overstimate these values. The LNS and the new hybrid model underestimate these values and the error seems to be higher than in DES with respect to experimental data. The Strouhal number obtained in the different simulations are very similar and close to the numerical value. The length of the recirculation bubble is similar for all the hybrid models excepted for DES2, which seems to gives a larger error in the estimation of the value. In Fig.3.21 the u velocity profiles on the plane y=0 obtained by the new hybrid model and the LNS are plotted togheter with those given by DES and the experiment.

It is possible to appreciate as there are no larger differences in the zone near the cylinder (except for DES2 that seems to overestimate the velocity). As already observed in Sec.3.2.1, LNS and the new hybrid model give a much higher recovery velocity with respect to the experiments while DES simulations does not have this problem. Maybe, this difference is not due by the model but by the dimension of the domain and by the boundary condition at the outflow.

It is important to underline that with the new code it is possible to obtain good results, comparable with those obtained with DES, but with smaller numerical resources.
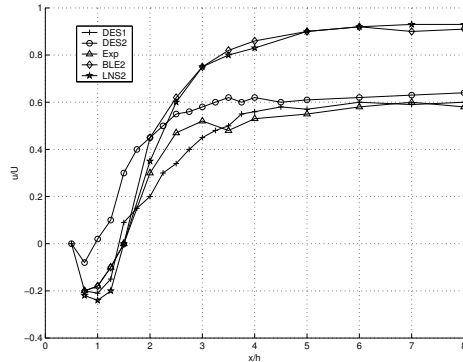

Figure 3.21. u velocity profiles for BLE1, LNS2, DES1, DES2 plane $y/L = 0$

Simulations	$\overline{C_d}$	C_d'	C_l'	St	l_r
LNS2	2.02	0.158	1.032	0.127	1.60
LNS3	2.11	0.116	0.654	0.131	1.15
LNS5	2.07	0.087	0.685	0.130	1.19
LNS6	2.08	0.086	0.628	0.136	1.01
BLE1	1.90	0.145	0.897	0.128	1.65
BLE2	1.95	0.107	0.810	0.130	1.37
BLE4	1.86	0.156	1.023	0.126	1.69
BLE5	2.01	0.117	0.792	0.131	1.16
BLE6	1.97	0.063	0.545	0.127	1.24
BLE7	2.01	0.074	0.580	0.129	1.13
BLE8	2.01	0.072	0.600	0.129	1.10
BLE9	2.01	0.071	0.600	0.131	1.21
BLE10	2.01	0.073	0.600	0.129	1.16
BLE11	2.01	0.083	0.630	0.128	1.05
BLE12	2.02	0.077	0.620	0.129	1.10
DES1 (Ref.[35])	2.42/2.57	0.28/0.68	1.36/1.55	0.09/0.13	1.16/1.37
DES2 (Ref.[25])	2.18			0.134	0.81
Exp.(Ref.[3])	2.28		1.2	0.130	
Exp.(Ref.[26])	2.1			0.132	1.4

Table 3.3.   Simulation results

Chapter 4

Flow around a circular cylinder

4.1 Description of the test case and of the simulation parameters

The flow around a circular cylinder of infinite length is considered. The Reynolds number, based on the cylinder diameter, D, and on the free-stream velocity, is equal to $Re_D = 140000$ and the used computational domain is represented in Fig. 4.1, together with the frame of reference. With reference to Fig. 4.1, the domain dimensions are the following: $L_i/D = 5$, $L_o/D = 15$, $H_y/D = 7$, $H_z/D = 2$ (where z is the spanwise direction). L_o and H_z are equal to those used in the DES simulations of *Travin et al.* [40].

The computational domain is discretized by generating a structured zone around the cylinder (Fig. 4.2 (b)), which has been divided in tetrahedrons by using the so called *English flag* division in order to make the grid compatible with the solver (which supports only tetrahedrical mesh). This structured zone has a diameter equal to $1.2D$; in the radial direction there are 25 logarithmically equally spaced points. Ten of these points are distributed in the zone $30 < y^+ < 300$; 180 and 40 nodes are in the azimuthal and spanwise directions respectively. In this zone, the maximum value of the stretching parameter of the cell (the ratio between the largest and smallest dimension of

the cell) is approximately 12.4. The unstructured grid covers the rest of the domain and it is more refined in the wake and in the upwind part close to the cylinder. The grid becomes progressively coarser moving towards the boundary of the domain. The section of the grid at $z = 0$ is reported in Fig. 4.2 (a). As for the square cylinder approximate boundary conditions, based on the Reichardt wall-law are applied at the solid walls. At the inflow, the flow is assumed to be rather turbulent by setting the inflow value of eddy-viscosity to about 5 times the molecular viscosity as in the DES simulation of Ref.[40]. This setting corresponds to a free-stream turbulence level $Tu = \overline{u'^2}/U_0$ (where u' is the inlet fluctuation velocity and U_0 is the free-stream mean velocity) of the order of 4%. As shown by *Zdravkovich* in Ref.[42], the effect of such a high level of free-stream turbulence is to make the boundary layer almost entirely turbulent also at the relatively moderate considered Reynolds number. Boundary conditions based on the Steger-Warming decomposition are used at the outflow. On the upper and lower surfaces ($y = \pm L_y$) slip conditions are imposed. Finally, the flow is assumed to be periodic in the spanwise direction in order to simulate a cylinder of infinite spanwise length.

The computations have been carried out using the new proposed hybrid model with the definition of the blending parameter based on the length ratio. The RANS model used is that based on the *Low Reynolds* approach discussed in Sec.1.2.2. The numerical parameter γ, which controls the amount of numerical viscosity introduced in the simulation, has been set equal to 0.2, in order to obtain stable simulations. The simulations have been implicitly advanced in time, with a maximum CFL number equal to 150. Because of the presence of significantly stretched elements of the grid, the *Barth* finite-volume cells have been used.
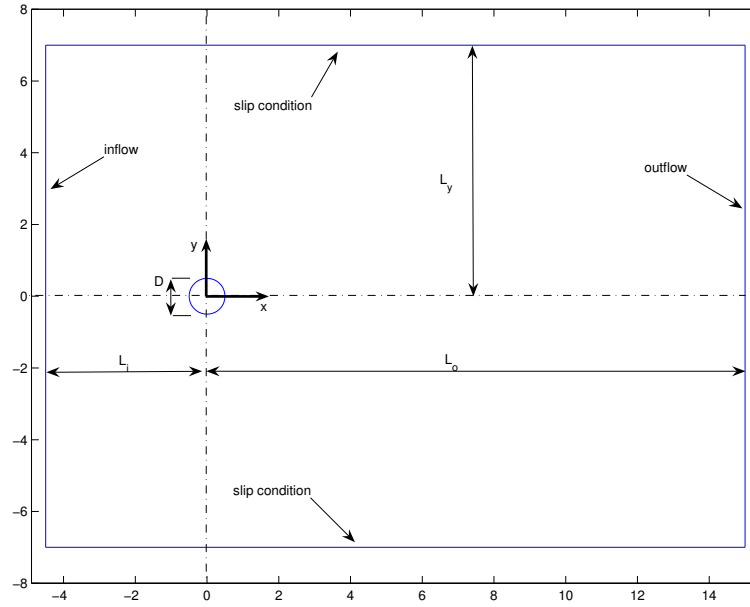
Figure 4.1.   Computational domain (side view)

L_i/D	L_o/D	L_y/D	L_z/D	N. nodes	N. elements
5	15	7	2	4.6×10^5	2.6×10^6

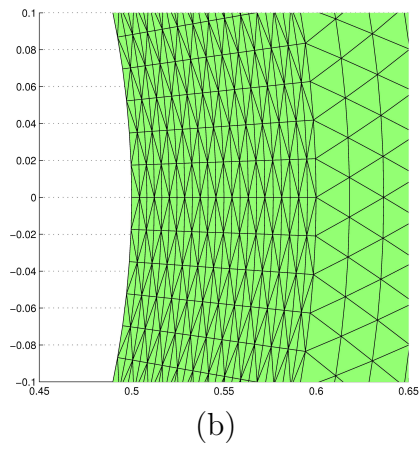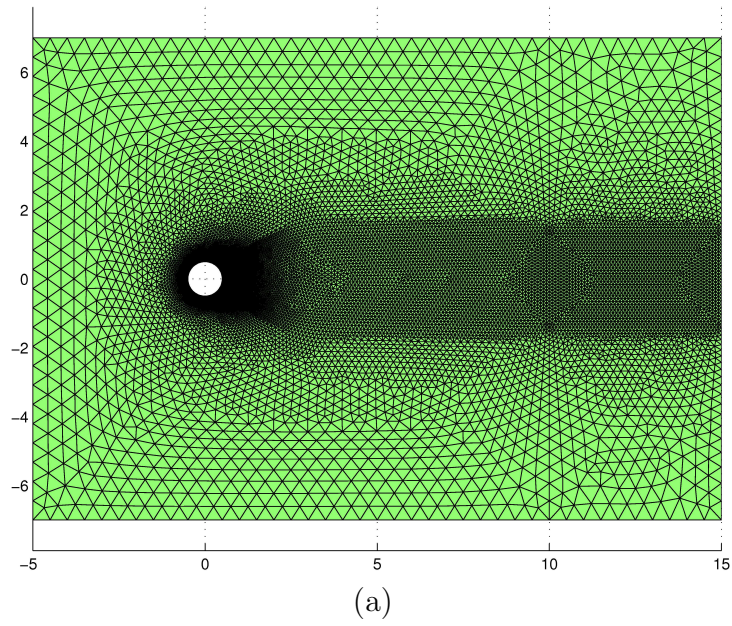Table 4.1.   Main feature of the computational domains and grids

(a)

(b)

Figure 4.2.   Section of the grid at $z = 0$ (a) and zoom of the structured zone (b)

4.2   Analysis of the results

The first step made in the post-processing phase is to understand if the boundary layer is effectively turbulent as expected. The ratio between the RANS viscosity and the molecular one, shown in Fig.4.3, is a parameter that can be used for this aim. Looking close to the cylinder wall, it is possible to see a red zone where the RANS viscosity is higher than the molecular one and that is a typical behavior of turbulent flows. Another parameter demonstrating that the boundary layer is turbulent, is the vorticity dispersion ratio (VDR) defined as:

$$VDR = \frac{C_{pb} - C_{pmin}}{1 - C_{pmin}}. \tag{4.1}$$

where C_{pb} is the base pressure coefficient and C_{pmin} is the minimum of the base pressure coefficient.

In the simulation VDR is equal to 0.45 that is a typical value for a circular cylinder having a turbulent boundary layer, as shown in Ref.[42].

4.2.1   Behavior of blending parameter

In Fig.4.4 the instantaneous isocontours of the blending parameter in the field are plotted. As seen in the case of square cylinder, where the parameter is close to one (red zones) the model works in RANS mode, where the parameter is close to zero (blue zones) the model works in VMS-LES mode and, for the other value between zero and one, the model works in a hybrid way. It is clear from Fig.4.4 that the model uses RANS close to the cylinder and out of the wake, VMS-LES in the wake, and a hybrid mode in the upwind part of the domain and in the transition zones. This is a qualitatively correct behavior and is in line with that observed in the case of the square cylinder in Sec.3.2. Although relative to a particular time instant, this picture is representative enough of the qualitative behaviour of the model during the
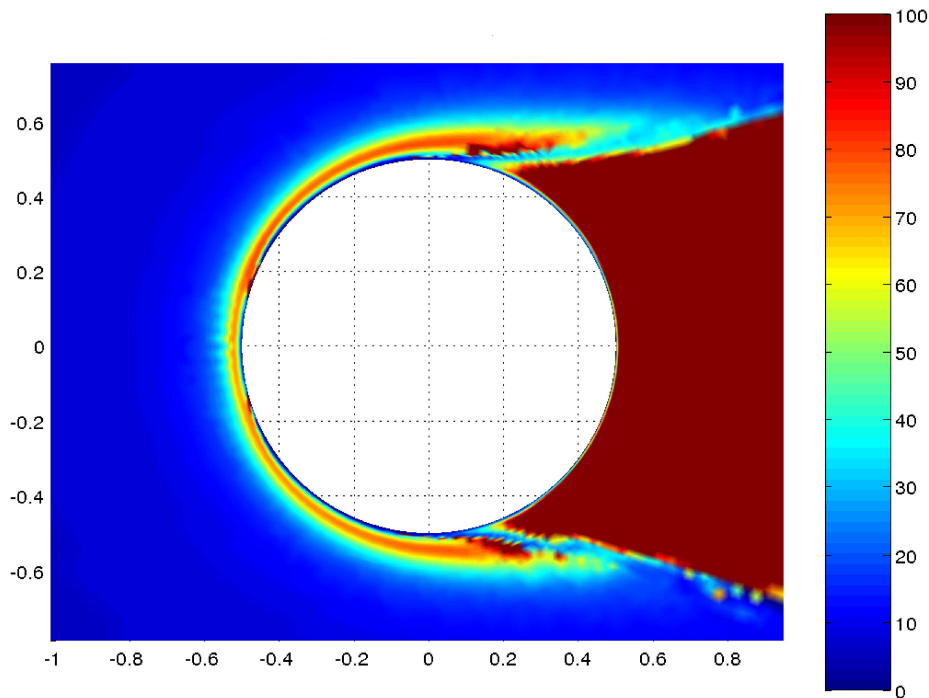
Figure 4.3.   Isocontours of the ratio between RANS and molecular viscosity

whole time history. In Fig.4.5 the mean resolved turbulent kinetic energy is plotted. This parameter is useful to see if the model has some zone where the transition between RANS to VMS-LES is smooth, as favorable, or not. Fig.4.5 (a) shows how effectively in the field there are no abrupt variation going out the wake (that is the zone where the model switches from VMS-LES to RANS). Also, in another critical transition part, the zone around the cylinder (Fig.4.5 (b)), where the gradient are also high, the transition is very regular and smooth. This is a positive feature that is not observed, for example, for DES. This model suffers in these zones (particularly near the shear layers) of the problem of *gray-area*, i.e. parts of the domain where the model is unable to set RANS or LES mode (Ref.[40]).
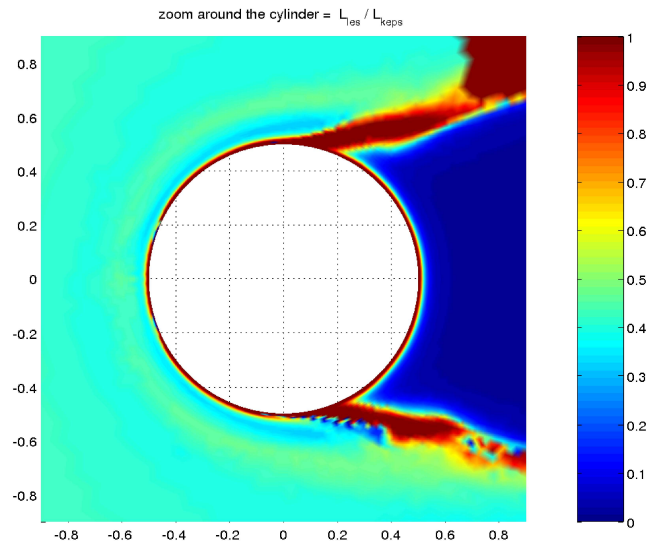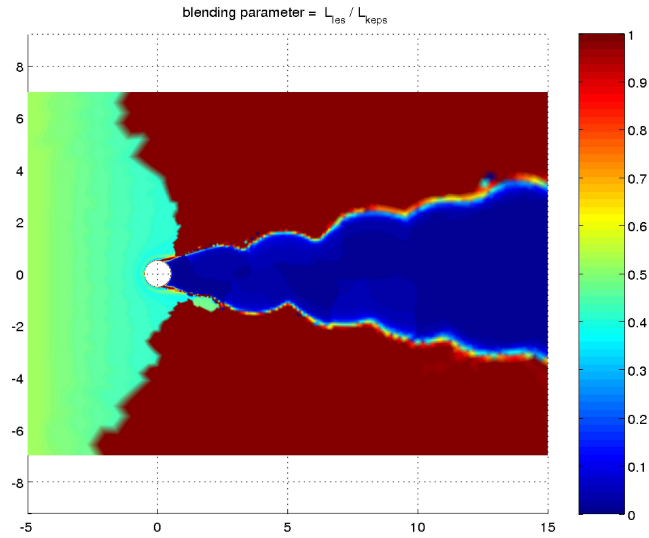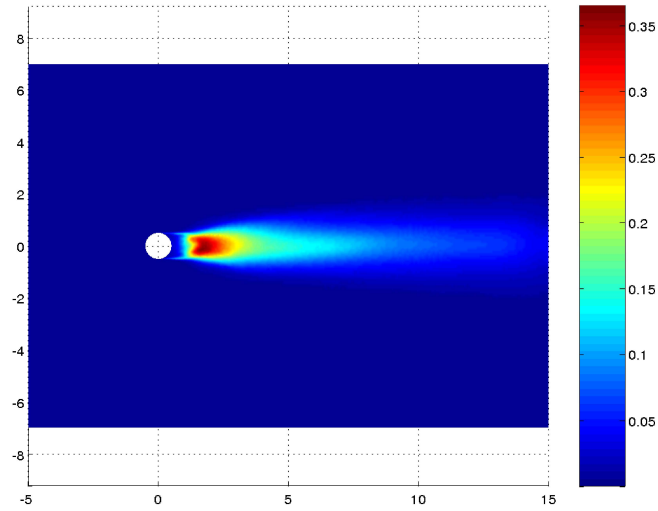
67

(a)

(b)

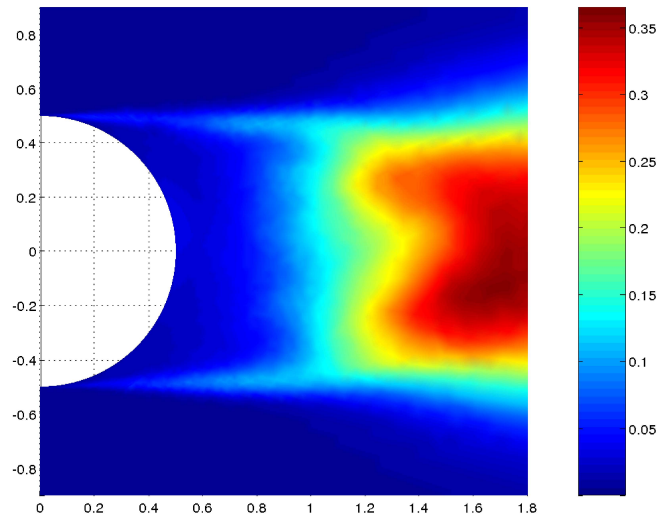Figure 4.4.   Blending parameter based on Length Ratio.

4.2.2   Comparison of numerical results

A brief summary of the global parameters used in our simulation and those of some experiments and numerical simulations, which will be used for comparison, can be found in Tab.4.2. Namely, the Reynolds number and, where

(a)

(b)

Figure 4.5. Turbulent kinetic energy field (a) and zoom around the cylinder (b).

available, the inlet turbulence level T_u are reported. The numerical simulations used for comparison are those made with the DES model by *Travin et al.* [40] and by *Lo et al.* [25]. These simulations have been carried out with the same Reynolds number and the same initialization of the inlet RANS

69

viscosity used in our simulation. The experimental data are divided in two categories. The first one (named LS, i.e. laminar boundary layer) reports the results at the same Re_D as in our simulations but with a significantly lower value of the free-stream turbulence level. In these experiments the boundary layer is not turbulent and, as shown in the following, the results are completely different from those obtained with our simulation. The second one (TS, turbulent boundary layer) reports the experimental data obtained at very high Reynolds number and low value of the free-stream turbulence level. These last experiments are used for comparison with our results as done by *Travin et al.* [40] and by *Lo et al.* [25].

Sim.	Re	T_u
CC140k	1.4×10^5	4%
Num. sim.		
Ref.[40]	1.4×10^5	high
Ref.[25]	1.4×10^5	high
Exp. sim.	LS	
Ref.[34]	1.4×10^5	0.4%
Ref.[1]	1.4×10^5	0.7%
Ref.[33]	1.4×10^5	low
Exp. sim.	TS	
Ref.[1]	5×10^6	0.7%
Ref.[19]	3.78×10^6	low
Ref.[20]	8×10^6	0.17%
Ref.[33]	8.4×10^6	low
Ref.[34]	8×10^6	0.4%
Ref.[31]	8×10^6	0.5%

Table 4.2. Parameters for numerical and experimental simulations.

In Tab.4.3 the obtained numerical results are compared with those obtained in experimental and numerical simulations are shown. The first observation is that, as we expected, the numerical results are close to the experimental data obtained at higher Reynolds number. Specifically it is possible to see that the mean drag coefficient($\overline{C_d}$) is in the range obtained in the considered experiments and close to that computed in DES. The r.m.s value of

lift (C'_l) and drag (C'_d) are close to the experimental ones and in line with the results of DES. Also, the base pressure coefficient (C_{pb}) is close to numerical data and slightly higher than that measured by *Jones et al.* (Ref.[20]) or that from *James et al.* (Ref.[19]), and lower than that reported by *Roshko* (Ref.[33]). The separation angle is also very close to the experimental data, more than the one obtained in the DES simulations of *Travin et al.* [40] and of *Lo et al.* Ref.[25]. The only value which is in disagreement with the DES results is the length of the recirculation bubble (l_r), which is much higher than that computed in the two numerical simulations. Unfortunately, for this parameter no experimental data have been found and thus it is not possible to understand which value is the best.

Sim.	$\overline{C_d}$	C'_d	C'_l	St	l_r	θ_{sep}	C_{pb}
CC140k	0.620	0.018	0.083	0.302	1.69	108	0.65
Num.	data	TS					
Ref.[40]	0.57/0.65		0.08/0.1	0.28/0.31	1.1/1.4	93/99	0.65/0.70
Ref.[25]	0.6/0.81			0.29/0.30	0.6/0.81	101/105	0.85/0.91
Exp.	data	LS					
Ref.[34]	1.2		0.26	0.2			
Ref.[1]	1.2					75	
Ref.[33]	1.2			0.2			-1.16
Exp.	data	TS					
Ref.[1]	0.7					112	
Ref.[19]	0.58			0.25		110	0.58
Ref.[20]	0.58			0.29		112	0.6
Ref.[33]	0.7			0.27		107	0.8
Ref.[34]	0.52		0.06	0.28			
Ref.[31]		0.016					

Table 4.3.   Simulation results comparison with numerical and experimental data.

In Fig.4.6 (a) and (b) the history of the lift and drag coefficient are reported respectively. Good agreement is obtained with experimental (from *Schewe* Ref.[34] Fig. 4.7(a)) and numerical values (from *Travin et al.* Ref.[40] Fig4.7(b)). In Fig.4.8 the distribution over the upper face of the cylinder of the mean value of the pressure coefficient ($\overline{C_p}$) is plotted. The agreement with

the experimental distribution is very good except for a slightly overestimated value of the $\overline{C_p}$ in the rear and in the front zone of the cylinder. This latter problem is due to the fact that $\overline{C_p}$ is higher than 1 at the stagnation point. This is a problem already found in previous simulations where no preconditioning has been used and could be arranged by using a suitable preconditioning (see, for istance, Ref.[14]). The value computed with the DES method by *Travin et al.* gives a better estimation in the front and rear part of the cylinder but the agreement with the experiments is more satisfactory with the presented model for $60^0 < \theta < 90^0$. In particular the minimum value seems to be better predicted by the new hybrid model.

In Fig.4.9 the mean skin friction coefficient ($\overline{C_f}$) is plotted; it has been computed as:

$$\overline{C_f} = \frac{\tau}{\rho U_0^2}, \quad \tau = \rho u_f^2 \tag{4.2}$$

where τ is the skin friction, u_f is the friction velocity that is an output of the wall-law model, ρ is the density and U_0 the free-stream velocity. The plotted value is far from the experimental one. On the other hand, the result is in accord with that from DES. As explained also in Ref.[40], this disagreement with the experiments is probably due to the fact that the experimental data are obtained at $Re_D = 3.6 \times 10^6$ and maybe at this Reynolds number the boundary layer is not completely turbulent. Unfortunately, also for this results no experiments at higher Reynolds are available. The computation of $\overline{C_f}$ becoms less satisfactory going near the separation point. This is maybe due to the fact that the wall-law (used to compute the value) does not work well near the separation zones.
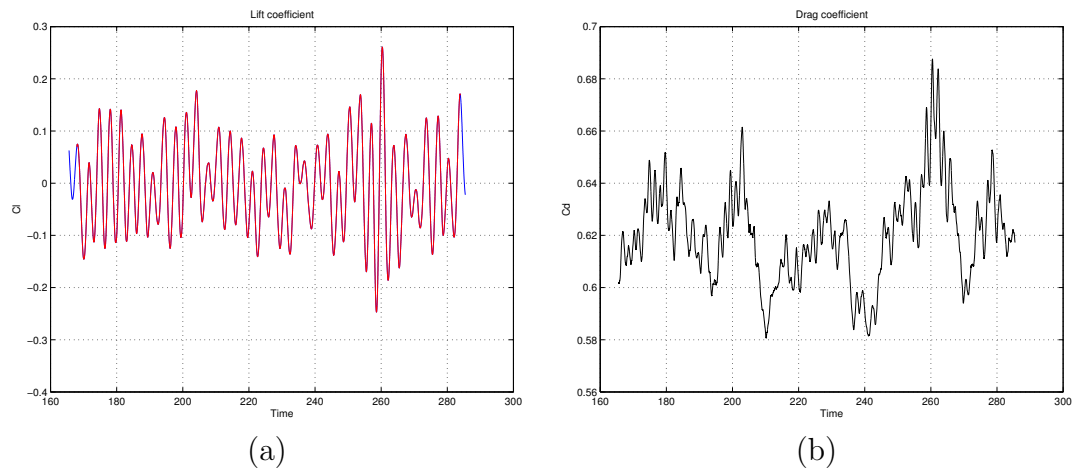
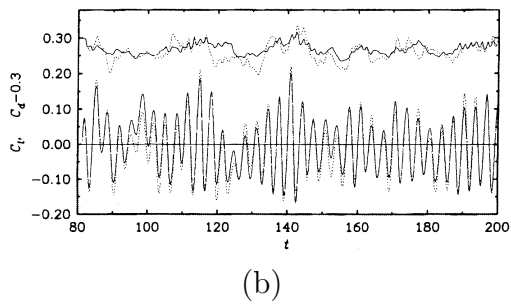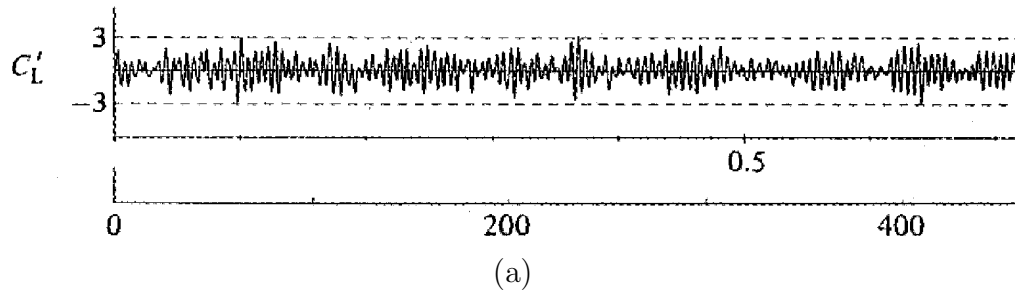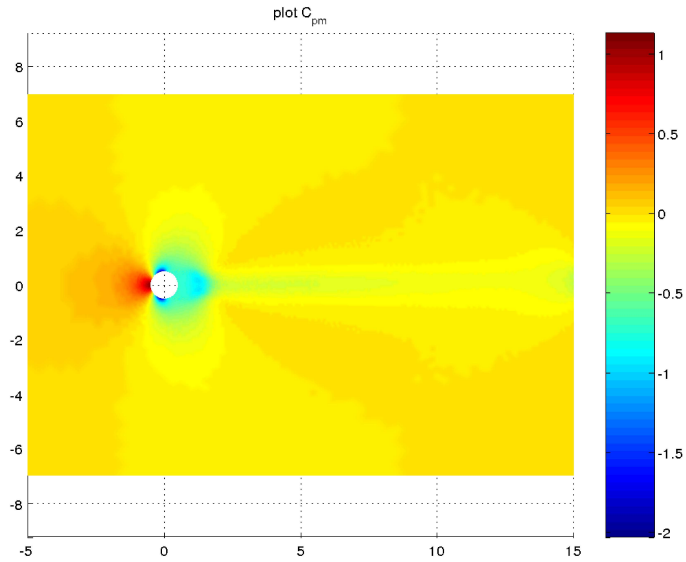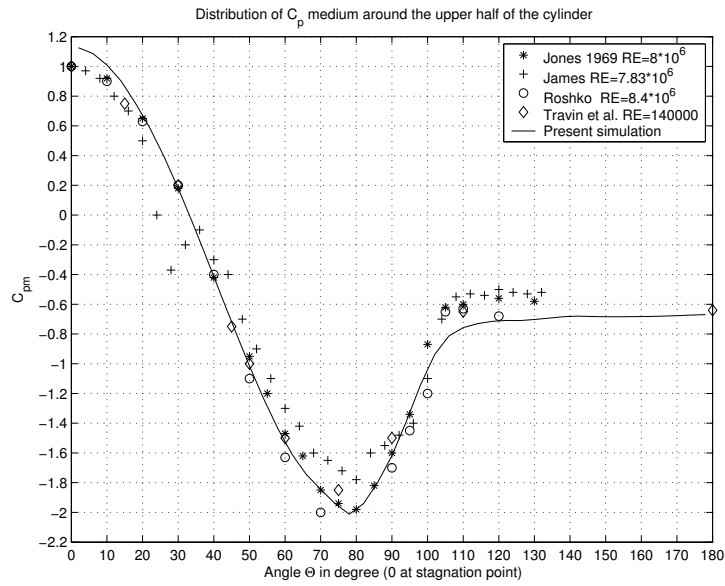Figure 4.6. C_l history (a), C_d history (b)

Figure 4.7.   *C_l history from Schewe* [34](a), *C_l and C_d history from Travin et al.* [40] (b)

73

(a)

(b)

Figure 4.8. C_p medium field (a) and distribution around the cylinder (b).

74

distribution of skin friction factor c_f
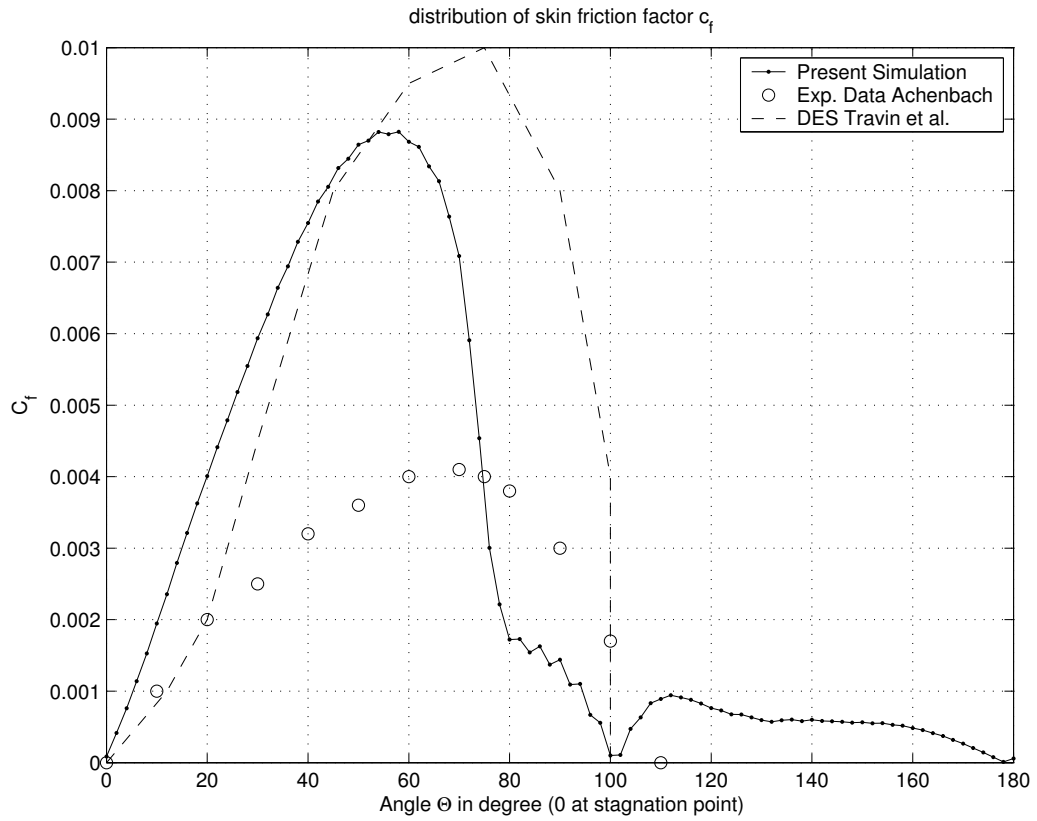
Figure 4.9. C_f distribution around the cylinder.

Chapter 5

Conclusions

A new strategy for blending RANS and LES approaches into an hybrid model has been presented, which is based on a decomposition of the flow variables in a RANS part (i.e. the averaged flow field), a correction part which takes into account the resolved turbulent scale fluctuations, and a third part made of the unresolved or SGS fluctuations. The RANS flow field is simulated and, where the grid is adequately refined, it is corrected by adding the resolved turbulent fluctuations. This is done by means of a blending function, such that the model coincides with the RANS approach where the grid is coarse and tends with continuity to the LES model as the grid is locally refined.

The proposed strategy is applied for blending the standard RANS $k - \varepsilon$ closure and the VMS-LES model with the Smagorinky closure. To this purpose, three different definitions of the blending function are tested.

The numerical discretization is based on a second-order accurate mixed finite-element/finite-volume method, applied to unstructured tetrahedral grids. It uses a sophisticated MUSCL reconstruction leading to a numerical viscosity made of sixth-order spatial derivatives. Either an explicit Runge-Kutta algorithm or a second-order time-accurate implicit scheme can be used to advance the equations in time.

The resulting hybrid RANS/VMS-LES method has been applied to the numerical simulation of a classical benchmark for bluff-body flows, i.e. the

flow around an infinite-length square cylinder at $Re = 22000$. For comparison, another hybrid model has been considered here, obtained by applying the LNS blending criterion, which is based on the ratio between the RANS and the LES viscosity, to blend the standard RANS $k - \varepsilon$ closure and the Smagorinsky model. A comparison with hybrid codes, based on DES model, has been also provided.

Simulations have been carried out on two grids having different spatial resolution; sensitivity of the results to the inlet turbulent kinetic energy and to the parameter δ in the approximate wall treatment have been also appraised.

For the tests carried out with the more refined grid it has been shown that the results of the new hybrid model are in accord with those computed with LNS and the agreement with experimental data is acceptable. Also in the coarser grid the LNS and the new hybrid model give comparable results, and the agreement with the experimental data is not completely satisfactory even if, as shown in [8], comparable to that of other LES simulations in the literature. The comparison with DES is also encouraging because the results are comparable but obtained with more limited numerical resources.

The results obtained for the selected test case did not seem to be sensitive to the different definitions of the blending function. This might be due to the fact that, in the considered flow, the boundary layer separation separation is fixed by the geometry and this might reduce the sensitivity of the results to the different choices in the turbulence model. However, from an a-posteriori analysis on the proposed blending functions, it is shown that, although empirically based, they lead to a sensible behavior, at least for the present test-case. Indeed, for all the grid resolutions, the new hybrid model works in LES mode in the separated unsteady wake, and this is consistent with the rationale of hybrid models.

It is finally shown that the sensitivity of the results to the inlet turbulent kinetic energy is low. This means that the proposed hybrid model counterbalance the potential negative effect on the results that could be generated

by the inaccurate prescription of the inflow turbulent kinetic energy. Conversely, it is shown that results are strongly affected by the parameter δ in the adopted wall-law, which consequently deserves a particular attention and a further investigation.

In addiction to the previous test case the flow around a circular cylinder, which is a challenging and widely studied flow, has been considered. The simulation has been carried out at $Re = 140000$. The inlet value of the kinetic RANS viscosity has been set to five times the molecular one to obtain a completely turbulent boundary layer.

In this case the *Low-Reynolds $k - \varepsilon$* model, has been blended with the VMS-LES model. The definition based on the ratio of the characteristic RANS and LES length has been used for the blending parameter.

The simulation has been carried out on a mixed structured-unstructured grid, with highly stretched cells in the zone near the cylinder wall. Because of this the Barth cell method has been used to avoid possible numerical problems.

The results have been compared with those obtained by a similar DES simulation and with experimental data.

The test has shown that the blending parameter used sets in the correct way the RANS and the LES zones. The only problem has been observed to be in the zone behind the cylinder where the transition from RANS to LES appears to occurs too downstream and thus maybe it is responsable of the overstimation of the length of the mean recirculation bubble.

However, the test has shown that the results obtained with the new hybrid model are comparable with those given by DES and with the experiments. Moreover some results (for example the estimation of the separation angle) are closer to experimental data than those computed with DES.

Bibliography

[1] E. Achenbach, *Distribution of local pressure and skin friction around a circular cylinder in croos-flow up to $Re = 5 \times 10^6$*, J. Fluid Mech., 34(4), (1968), 625-639.

[2] P. Batten, U. Goldberg and S. Chakravarthy, *Interfacing statistical turbulence closures with large-eddy simulation*, AIAA Journal, 42(3), (2004), 485-492.

[3] P.W. Bearman and E.D. Obasaju, *An experimental study of pressure fluctuations on fixed and oscillating square-section cylinders*, J. Fluid Mech., 119, (1982), 297-321.

[4] G. Bosh and W. Rodi, *Simulation of vortex shedding past a square cylinder with different turbulence models*, Int. J. Num. Meth. Fluids, 28, (1998), 601-616.

[5] S. Camarri, B. Koobus, M. V. Salvetti and A. Dervieux , *A low diffusion MUSCL scheme for LES on unstructured grids*, Technical Report RR-4512, INRIA, (2002).

[6] S. Camarri, B. Koobus, M. V. Salvetti and A. Dervieux , *Large-Eddy simulation of a bluff-body flow on unstructured grids*, Int. J. Num. Meth. Fluids, 40, (2002), 1431-1460.

[7] S. Camarri, M. V. Salvetti, B. Koobus and A. Dervieux , *A low diffusion MUSCL scheme for LES on unstructured grids*, Computers and Fluids, 33, (2004), 1101-1129.

[8] S. Camarri, M. V. Salvetti, B. Koobus and A. Dervieux , *Hybrid RANS/LES simulations of a bluff-body flow*, Wind and Structures, 8,

(2005), 407-426.

[9] *Cobalt user's manual, Cobalt Ver. 2.0*, Cobalt Solution, LLC, Springfield, OH.

[10] H.A. Dwyer and W.J. McCroskey, *Oscillating flow over a cylinder at large Reynolds number*, J. Fluid Mech., 61, (1973), 753-767.

[11] C. Farhat, B. Koobus and H. Tran, *Simulation of vortex shedding dominated flows past rigid and flexible structures*, In Computational Methods for Fluid-Structure Interaction, Tapir, (1999), 1-30.

[12] U. Goldberg, O. Peroomian, S. Chakravarthy, *A wall-distance-free $k-\varepsilon$ model with Enhanced Near-Wall Treatment*, Journal of Fluids Engineering, 120, (1998), 457-462.

[13] N. Gourvitch, G. Rogé, I. Abalakin, A. Dervieux and T. Kozubskaya, *A tetrahedral-based superconvergent scheme for aeroacoustics*, INRIA Report, RR-5212 (2004).

[14] H. Guillard and C. Viozat , *On the behaviour of upwind schemes in the low Mach number limit*, Computers and Fluids, 28, (1999), 63-86.

[15] J. Hinze, *Turbulence*, MacGraw-Hill, New York, (1959).

[16] T.J.R. Hughes, L. Mazzei and K.E. Jansen. *Large eddy simulation and the variational multiscale method*, Comput. Vis. Sci., 3, (2000), 47-59.

[17] A.N. Kolmogorov, *The local structure of turbulence in incompressible viscous fluid for very large Raynolds numbers* Dakl. Akad. NankSSR30, 299-303.

[18] B. Koobus and C. Farhat, *A variational multiscale method for the large eddy simulation of compressible turbulent flows on unstructured meshes-application to vortex shedding*, Comput. Methods Appl. Mech. Eng., 193, (2004), 1367-1383.

[19] W.D. James, S.W. Paris and G.V. Malcolm *Study of viscous cross flow effects on circular cylindes at high Reynolds numbers*, AIAA Journal, 18, (1980), 1066-1072.

[20] G.W. Jones, J.J. Cincotta and R.W. Walker, *Aerodynamic forces on*

a stationary and oscillating circular cylinder at high Reynolds numbers, National Aeronautics and Space Administration, NASA TR R-300, (1969).

[21] J. Jones and B.E. Launder, *The prediction of laminarization with a two-equation model of turbulence*, Int. J. Heat and Mass Tensf., 15, (1972), 301-314.

[22] E. Labourasse and P. Sagaut. *Reconstruction of turbulent fluctuations using a hybrid RANS/LES approach*, J. Comp. Phys., 182, (2002), 301-336.

[23] M.H. Lallemand, H. Steve and A. Dervieux. *Unstructured multigridding by volume agglomeration: current statuts*, Comput. Fluids, 21, (1992), 397-433.

[24] B.E. Launder and D.B. Spalding, *The numerical computation of turbulent flows*, Comp. Meth. Appl. Mech. and Eng., 3, (1979), 269-289.

[25] S.-C. Lo, K.A. Hofmann and J.-F. Dietiker, *Numerical investigation of High Reynolds Number Flows over Square and Circular Cylinder*, Journal of Thermophysics and Heat Transfer, 19, (2005), 72-80.

[26] D.A. Lyn and W. Rodi, *The flapping shear layer formed by flow separation from the forward corner of a square cylinder*, J. Fluid Mech., 267, (1994), 353-376.

[27] R. Martin and H. Guillard , *A second order defect correction scheme for unsteady problems*, Computers and Fluids, 25(1), (1996), 9-27.

[28] B. Mohammadi and O. Pironeau , *Unsyteady separated turbulent flows computation with wall-laws and $k - \varepsilon$ model*, Comput. Method Appl., 148(3-4), (1997), 393-405.

[29] B. Mohammadi and G. Medic , *A critical evaluation of the classic $k - \varepsilon$ model and wall-laws for unsteady flows over bluff bodies*, Int. J. Comp. Fluid. Dyn., 10(1), (1998), 1-11.

[30] R. Peyret, *Handbook of computational fluid mechanics*, Academic Press, 2004

[31] A. Richter and E. Naudascher, *Fluctuation forces on a rigid circular*

cylinder in confined flow, J. Fluid Mech., 78, (1976), 561-576.

[32] P. L. Roe, *Approximate Riemann solvers, parameters, vectors and difference schemes*, J. Comp. Phys., 43, (1981), 357-372.

[33] A. Roshko, *Pressures and Forces on a circular cylinder in cross flow at high Reynolds numbers*, J. Fluid Mech., 10, (1961), 345-356.

[34] J.W. Schewe, *On the forcesacting on a circular cylinder in cross flow from subcritical up to transcritical Reynolds numbers*, J. Fluid Mech., 133, (1983), 265-285.

[35] S. Schmidt and F. Thiele, *Comparison of numerical methods applied to the flow over wall-mounted cubes*, Int. J. of Heat and Fluid Flow, 23, (2002), 330-339.

[36] J. Smagorinsky, *General circulation experiments with the primitive equations*, Monthly Weather Review, 91(3), (1963), 99-164.

[37] P.R. Spalart and S.R. Allamaras, *A one-equation turbulence model for aerodynamic flows*, La Rech. Aerospatiale, 1 , (1994), 5-21.

[38] P.R. Spalart and S.R. Allamaras, *Extensions of the Spalart-Allmaras turbulence model to account for wall roughness*, International Journal of Heat and Fluid Flow, 24 , (2003), 454-462.

[39] J.L. Steger and R.F. Warming, *Flux vector splitting for the inviscid gas dynamic equations with applications to the finite difference methods*, J. Comp. Phys., 40(2), (1981), 263-293.

[40] A. Travin, M. Shur, M. Strelets and P. Spalart, *Detached-Eddy Simulations Past a Circular Cylinder*, Flow, Turbulence and Combustion, 63, (1999), 293-313.

[41] P. van Leer, *Towards the ultimate conservative scheme. IV: A new approach to numerical convection*, J. Comp. Phys., 23, (1977), 276-299.

[42] M.M. Zdravkovich, *Flow around circular cylinders*, Oxford University Press, (2003).